


Article

Computational Analysis of Aerodynamic Blade Load Transfer to the Powertrain of a Direct-Drive Multi-MW Wind Turbine

Magnus Bichan *, Pablo Jaen-Sola , Firdaus Muhammad-Sukki  and Nazmi Sellami 

School of Computing, Engineering and the Built Environment, Edinburgh Napier University, 10 Colinton Road, Edinburgh EH10 5DT, UK; p.sola@napier.ac.uk (P.J.-S.); f.muhammadsukki@napier.ac.uk (F.M.-S.); n.sellami@napier.ac.uk (N.S.)

* Correspondence: m.bichan@napier.ac.uk

Abstract

This paper details the development of a full turbine model and ensuing aero-servo-elastic analysis of the International Energy Agency's 15MW Reference Wind Turbine. This model provides the means to obtain realistic turbine performance data, of which normal and tangential blade loads are extracted and applied to a simplified drivetrain model developed expressly to quantify the shaft eccentricities caused by aerodynamic loading, thus determining the impact of aerodynamic loading on the generator structure. During this process, a method to determine main bearing stiffness values is presented, and values for the IEA-15MW-RWT obtained. It was found that wind speeds in the region of turbine cut-out induce shaft eccentricities as high as 56%, and that tangential loading has a significant contribution to shaft eccentricities, increasing deflection at the generator area by as much as 106% at high windspeeds, necessitating its inclusion. During a subsequent generator structure optimisation, the shaft eccentricities caused by the loading scenarios examined in this paper were found to increase the necessary mass of the rotor structure by 40%, to meet the reduced airgap clearance.

Keywords: direct-drive wind turbine; aero-servo-elastic analysis; aerodynamic load transfer; simplified powertrain design; generator structure optimisation



Academic Editor: Ahmed Abu-Siada

Received: 22 April 2025

Revised: 26 June 2025

Accepted: 29 June 2025

Published: 2 July 2025

Citation: Bichan, M.; Jaen-Sola, P.; Muhammad-Sukki, F.; Sellami, N. Computational Analysis of Aerodynamic Blade Load Transfer to the Powertrain of a Direct-Drive Multi-MW Wind Turbine. *Machines* **2025**, *13*, 575. <https://doi.org/10.3390/machines13070575>

Copyright: © 2025 by the authors. Licensee MDPI, Basel, Switzerland. This article is an open access article distributed under the terms and conditions of the Creative Commons Attribution (CC BY) license (<https://creativecommons.org/licenses/by/4.0/>).

1. Introduction

The growing climate crisis, and desire for energy autonomy, has spurred a flurry of activity and progress in the development and deployment of renewable energy globally, with global investment in low-carbon technologies breaching USD 1 trillion in 2023 [1] and the installed capacity of wind energy alone surpassing 272 GW in Europe as of 2023 [2]. Venturing offshore represents an opportunity to capitalise on higher wind energy capacity factors, enabled by steadier and stronger winds, and in a reflection of the technological advancements made in the field, and the desire for more dependable, predictable generation, 21% (3.8 GW) of the new European wind energy capacity came from offshore wind farms in 2023 [2].

Thanks to the significant investment the industry has received in recent years, offshore wind has seen an impressive reduction in the levelised cost of energy (LCOE) and is projected to reach parity with large-scale solar and onshore wind by 2025 [3]. Research suggests however, that economies of scale for offshore wind favour the upscaling of individual turbines, not the size of the overall wind farm [4]. Examining the UK's renewable energy pipeline shows this to be true, as the average capacity of wind turbines in operation

offshore, as of June 2024, is 5.1 MW, progressing to 9.0 MW in projects currently under construction and reaching 13.4 MW for approved projects awaiting construction [5]. These figures have grown in the brief time from April of 2023, when the average size of turbines for projects approved and awaiting construction was 10.7 MW [6]; furthermore, commercially deployed turbines have reached 14.7 MW [7] and operating demonstration turbines have surpassed sizes of 14.7 [8] to 16 MW [9].

Alongside the desire for ever larger turbines to reduce capital expenditure, the minimisation of operation and maintenance (O&M) costs is a key factor in reducing the LCOE of offshore wind. Remoteness and adverse weather conditions both work to reduce the available working hours for the maintenance and repair of offshore turbines, whilst the need for additional qualifications to work offshore, and to house those employees in service operation vessels, both increase the cost of labour. Jack-up vessel hire, used during installation and for the replacement of large components, likewise acts to increase operation costs. The net result is that O&M can account for 23% [10] to 35% [11]; while O&M costs onshore can be as little as 5% [10], vessel hire alone can contribute as much as 73% of the O&M costs of offshore windfarms [12]. Avoiding instances of component failure where jack-up vessels would be required to facilitate replacement is a straightforward means to reducing O&M costs, and hence the LCOE of offshore wind. Moreover, with the move to ever larger offshore turbines, the need to minimise downtime is further amplified as fewer, larger turbines means a larger proportion of the overall windfarm output can be lost by the malfunction of one turbine.

As such, permanent magnet direct-drive (PMDD) has emerged as a leading method by which to reduce maintenance, turbine downtime and instances of major component replacements; reference [13] finds that gearbox failure is directly responsible for one third of all downtime offshore and that gearbox failures have, in the past, led to additional generator failures. By removing the gearbox from the drivetrain entirely, in favour of a direct linkage from the wind turbine rotor to the generator, the mechanical complexity of the system overall is greatly reduced, and a considerable source of downtime is eliminated.

However, as illustrated by Equation (1), (see Section 2.6.1) the intrinsic low-speed operation of direct-driven devices requires significantly higher torques to generate the same power output. Equation (2) establishes that the most immediate method to increase generator power output is to increase its radius.

Consequently, PMDD generators are both considerably bulkier and heavier when compared to geared transmission systems and necessitate increased and more complex structural support, whilst elevating capital cost. The structural optimisation of these devices has therefore become a key area of research, though with the high capital costs of PMDD generators, ensuring mass savings can be unlocked safely, without the risk of compromising the generator structures' integrity, is of the upmost importance.

Alongside conventional methods to optimise large-scale PMDD generator structures such as parametric and topology optimisation techniques, more recent efforts have involved the use of additive manufacturing to enable advanced topologies [14] and mathematically generated structures to minimise structural mass [15]. Efforts have also been made with the aim to examine and accurately account for the loads experienced by direct-drive wind turbine generator structures in their optimisation [16,17], and this is essential to designing and optimising materially efficient generator supporting structures, that conform to strict deformation limits whilst minimising capital expenditure.

In this paper, the aero-servo-hydro elastic simulation of an onshore version of the IEA-15MW-RWT was developed in the industry standard software QBlade CE (v 2.0.5.1) [18] to gain aerodynamic blade loading data, using wind field data generated and validated in QBlade. This was then applied in finite element analysis (FEA) to a simplified computer-

aided design (CAD) model within SolidWorks (v 29.3.0.0059) [19]. The simulation was performed in accordance with the process carried out in [20]. Through this, the impact of shaft deflections arising from aerodynamic normal and tangential loading on the airgap stability of the direct-drive generator can be obtained and hence accounted for in its design. This process was developed with the aim to enable a computationally efficient means to account for external loading in the design of the IEA-15MW-RWT direct-drive generator, and as such, the computational time requirements of the QBlade model developed in this paper are evaluated against more complex, offshore models published subsequent to its development. In developing the simplified structural model, this paper also presents a detailed specification of the two main drivetrain bearings of the IEA-15MW-RWT, and a method used to calculate their constant stiffness values.

This research addresses a critical gap in the wind energy literature by providing a comprehensive quantitative assessment of how aerodynamic blade loading patterns transfer through the drivetrain to affect generator structural integrity in next-generation turbines of the 15 MW class. While previous studies of this turbine class have examined either aerodynamic loading or generator structural design in isolation, this work uniquely bridges these domains through a coupled analysis methodology that preserves the dynamic and asymmetric nature of the loading conditions. The integration of QBlade aero-servo-elastic simulation data with detailed structural modelling reveals previously unidentified critical loading scenarios that occur due to the combination of normal and tangential forces. These findings challenge conventional design approaches that have neglected aerodynamic forces in their loading assumptions and demonstrate that the accurate prediction of structural behaviour requires consideration of the full spectrum of dynamic loading conditions experienced throughout the turbine's operational envelope. By quantifying the specific impact of tangential loading on structural deformation limits, this research provides valuable design guidance that will enable more reliable and material-efficient direct-drive generator structures for the next generation of large-scale offshore wind turbines.

2. Materials and Methods

This paper aims to establish the effects of aerodynamic loading transfer from the IEA-15MW-RWT rotor to its electrical generator under realistic weather conditions, and in striving to do so, this work is comprised of two distinct sections: the first details the development of an aero-servo-elastic simulation of the IEA-15MW-RWT, created in QBlade, using data available from the reference turbine's GitHub repository (v1.1) and corresponding technical report [21]. The second section describes the simplified drivetrain model produced in SolidWorks, expressly for the purposes of accurately modelling the application and transmission of aerodynamic loads, obtained from QBlade, to the generator.

2.1. The IEA 15MW Reference Wind Turbine

The IEA-15MW-RWT is a monopile fixed-bottom, variable speed, permanent magnet direct-drive, IEC Class 1B turbine, with a hub height of 150m and a specific power rating of 332 Wm^{-2} . It comprises a standard upwind, 3-bladed rotor arrangement with a blade length of 117 m and a rotor diameter of 240 m, and operates between cut-in, rated, and cut-out wind speeds of 3 ms^{-1} , 10.59 ms^{-1} and 25 ms^{-1} , respectively. The horizontal axis wind turbine (HAWT) has a minimum rotor speed of 5.0 rpm, and a maximum rotor speed of 7.56 rpm, which is maintained via collective pitch at above rated wind speeds [21].

2.2. Simplified IEA-15MW-RWT Model Development in QBlade

QBlade is an open-source software that enables the rapid production of both vertical axis (VAWT) and HAWT prototypes, and the evaluation of their performance through

aero-hydro-servo-elastic simulations. Whilst HAWTs dominate utility-scale applications (typically 1MW or greater with rotor diameters in excess of 120 m), VAWTs such as the Darrius turbine explored in [22] show potential for urban and small-scale development. Reference [23] presents a case study demonstrating the successful application of QBlade in conjunction with three distinct optimisation methods for the aerodynamic optimisation of an HAWT. QBlade uses Unsteady Blade Element Momentum (U-BEM) theory to calculate rotor performance and compute the loads acting on the rotor according to both the aerodynamic conditions and the form and aerodynamic properties of spanwise-discretised blade sections, whilst correcting for three-dimensional effects using the Prandtl Tip Loss Factor [24], and a 3D correction factor presented in [25]. U-BEM differs from classic Blade Element Momentum theory in that U-BEM is capable of transient-state simulation, providing the ability to incorporate phenomena that have a significant influence on turbine performance, such as turbulence and blade–tower interactions, thus providing greater insight into turbine behaviour than classic BEM theory can.

To suit the purposes of this work and with computational sustainability in mind, an onshore version of the IEA-15MW-RWT was developed, shown in Figure 1, using data available from the IEA GitHub repository [26], and in the Technical Report [21]. In order to capture unsteady phenomena at each discretised blade section, it is necessary to incorporate both a global coordinate system and local coordinate systems along the span of each blade, as can be seen in Figure 1.

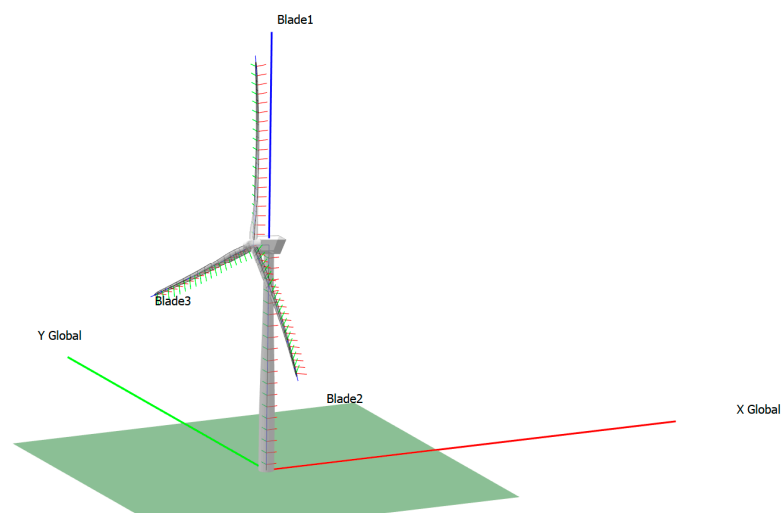


Figure 1. Onshore QBlade model, with global and local coordinate systems.

The DTU FFA-W3 series airfoil sections and their polars were obtained from the GitHub repository and defined in 50 discretised sections using the blade. Structural properties and performance characteristics, likewise obtained through documentation in the GitHub repository, were defined through the simulation modules' structural input files manually and are correspondingly defined at the 50 discretised airfoil sections, using local coordinate systems. The configurations of the blades as defined in the turbine definition document and in QBlade, are listed in Appendix A Table A1, while the discretised blade can be seen in Figure 2 and the blade's thrust and power coefficient values are displayed in Figure 3.

The mass densities and stiffness properties of the blade produced in QBlade are compared against those from the definition document [21] in Figures 4–6.

It can be seen that all parameters follow those outlined in the definition documentation closely, though the aero-servo-elastic model marginally underestimates mass density in the first 10% of the blade span (Figure 4), and edge stiffnesses is higher than that of the

definition documentation between 10 and 60% of the blade span (Figure 5), whilst axial stiffness (Figure 6) most closely tracks that of the turbine in the definition document.

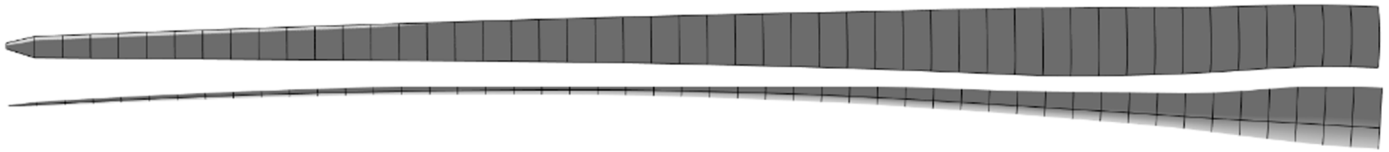


Figure 2. QBlade discretised IEA-15MW-RWT blade.

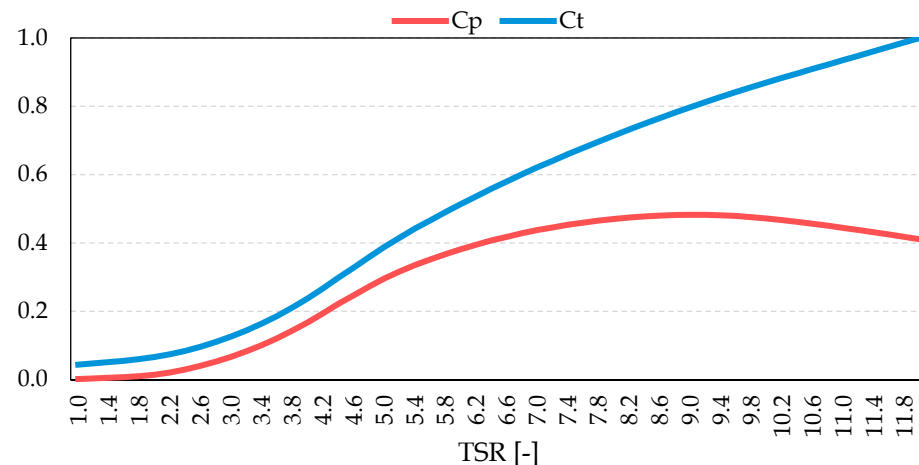


Figure 3. C_p and C_t values of the IEA-15MW-RWT blade obtained from QBlade.

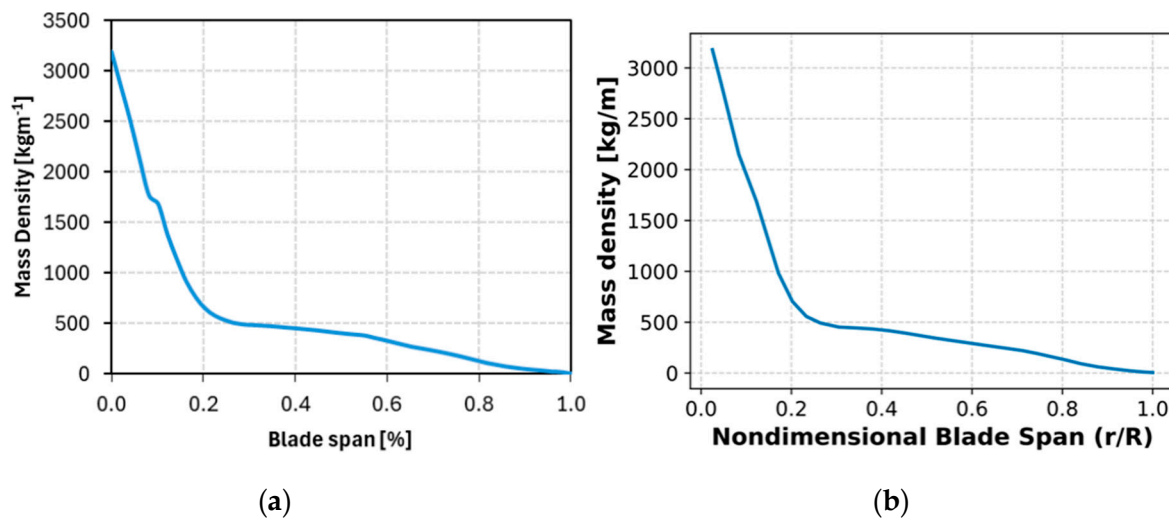


Figure 4. Blade mass density comparison between (a) Developed aero-servo-elastic model and (b) definition documentation [21].

The open source DTU Wind Energy Controller [27] was used alongside a DISCON parameter file, modified according to data published in the IEA-15MW-RWT GitHub repository, to define the turbines' elastic behaviour in given weather conditions. All QBlade simulations were given a run time of 10 min, and a timestep size of 0.125 s, resulting in 4800 total timesteps, as this was thought to provide adequate transient performance data.

Wind fields in QBlade are generated procedurally using NREL's stochastic, full-field turbulence simulator TurbSim [28], according to the turbines' hub height and user-determined mean wind speeds and grid sizes. Importantly, an examination of the wind fields produced in QBlade showed that outputs are identical regardless of whether the turbine is situated onshore or offshore, when provided identical inputs. Two main transient

loading conditions were examined: ‘Rated’, with a mean wind speed at the hub equal to the turbine’s rated wind speed of 10.6 ms^{-1} , and ‘High’, with a mean wind speed of 21 ms^{-1} . Mean windspeeds above 21 ms^{-1} were found to activate the turbine controller shut-off, as variance within the wind field was found to exceed the cut-out wind speed of 25 ms^{-1} and activate the turbine shut-off sequence. Both wind fields have a width of 300 m, height of 250 m and a hub height of 150 m, with a reference height of 150 m. The Kaimal turbulence model was used, and the duration was set to 2 min with stitching set to periodic. The ‘Rated’ wind field can be seen in Figure 7, where red peaks represent areas of higher windspeeds, and blue troughs are areas of lower windspeeds.

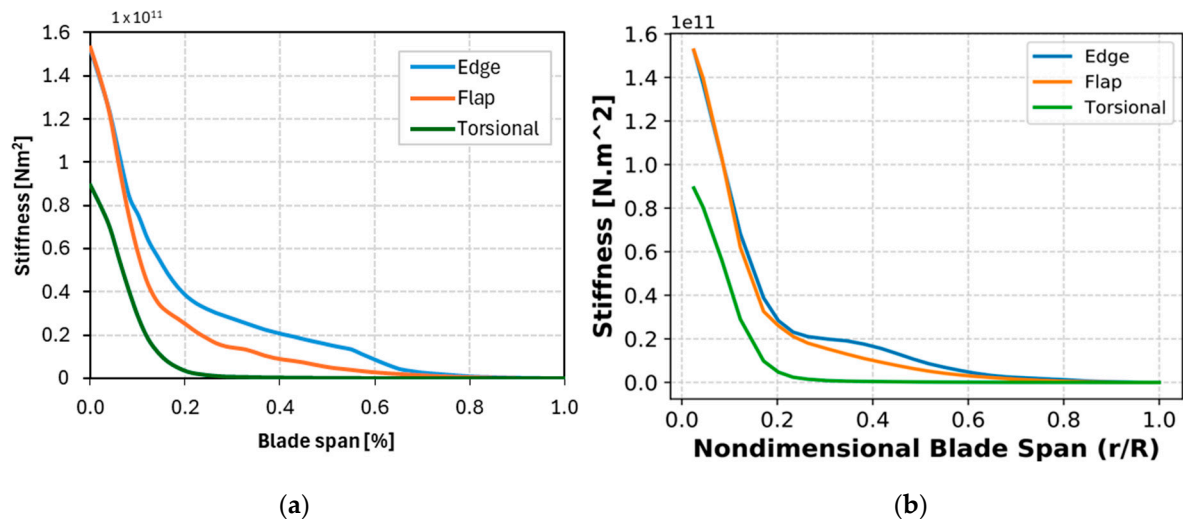


Figure 5. Blade edge, flap and torsional stiffness comparison between (a) developed model and (b) definition documentation [21].

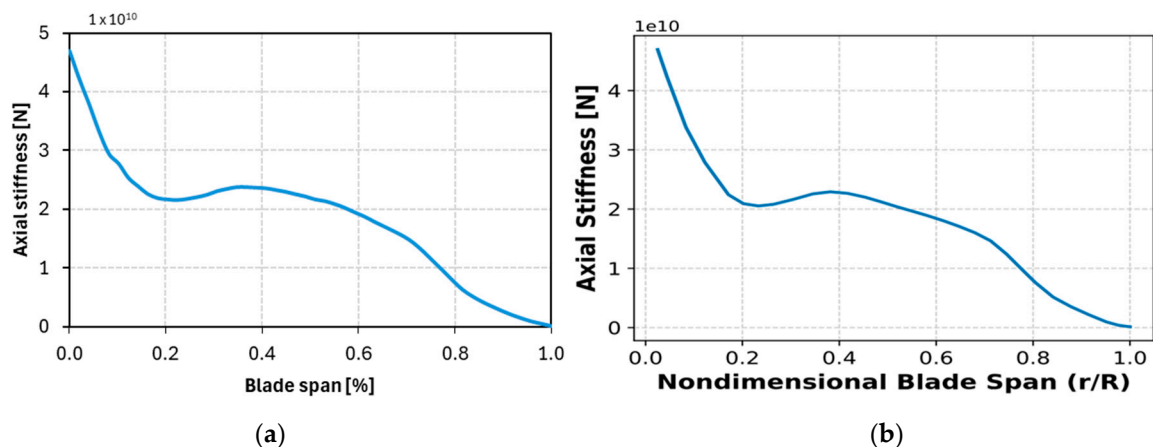


Figure 6. Blade axial stiffness comparison between (a) developed model and (b) definition documentation [21].

Initially, the normal and tangential forces across the span of each blade experienced under ‘Rated’ and ‘High’ conditions (seen in Figure 8) were obtained from the final timestep of each simulation; however, to account for a potential worst-case loading scenario, a full analysis of the aerodynamic loads was carried out. Under both ‘Rated’ and ‘High’ conditions, the total normal load on each blade was summed at each timestep, and the timestep corresponding to the highest total normal aerodynamic load across all 3 blades was found. The aerodynamic loads for each blade at that timestep were then obtained in 20 discretised sections, allowing the load profile to be replicated in the subsequent structural analysis. The distributed tangential

loads for each blade at that timestep were likewise collected, and the process was then repeated to find the timestep with the highest total tangential load and the corresponding distributed normal and tangential loads at that timestep were obtained.

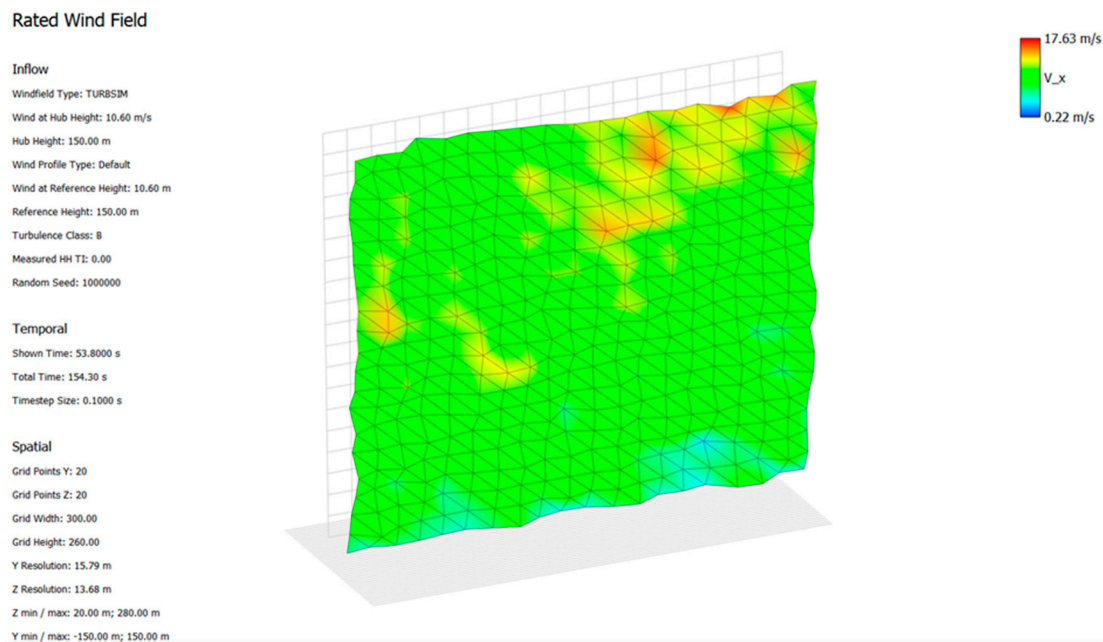


Figure 7. Graph of the wind field at 'Rated' conditions.

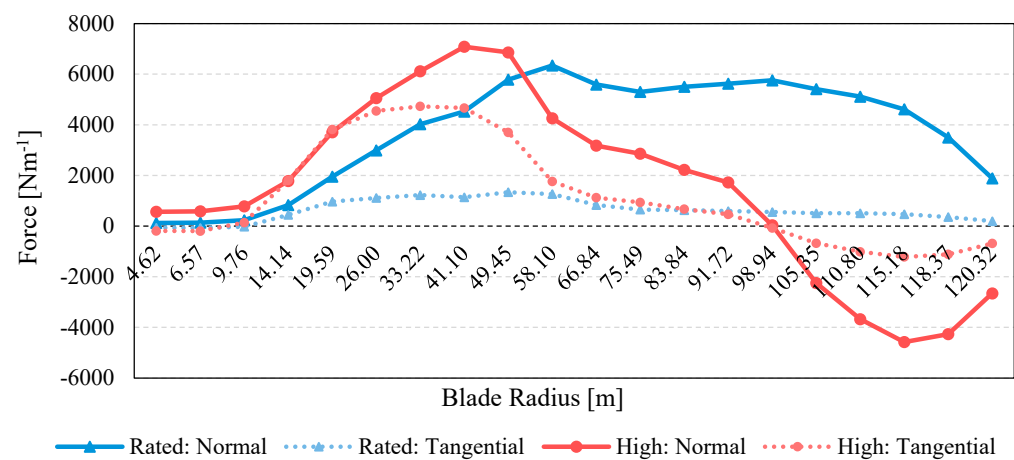


Figure 8. Blade 1 loading vs. blade radius at the final timestep for 'Rated' and 'High' settings.

To facilitate the comparison of the model developed in this paper against the floating and fixed-bottom models later published and made available for download by QBlade, the wind field hub and reference heights were increased to reflect the increase in the height of their fixed and floating offshore structures, and ensure each model is subject to the same loading conditions.

2.3. Simplified Drivetrain Model

To provide a means by which to obtain shaft displacements arising from aerodynamic blade loads, a simplified blade-and-driveshaft model was developed in SolidWorks. For the blades, shelled rectangular beams were created, allowing for an easy definition and application of aerodynamic loads, and each blade was discretised into 20 sections equal in length to the corresponding sections given by the QBlade output file, as can be seen in

Figure 9. As defined in the IEA documentation [21], these beams were 117 m in length, though their widths and breadths were taken as the average of the blade's span.

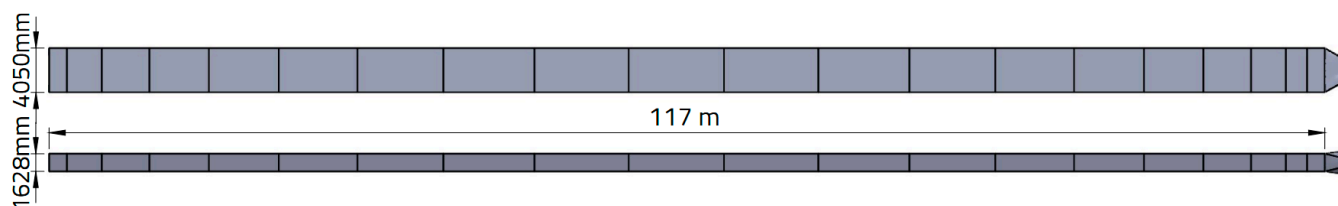


Figure 9. Simplified blade structure: front (top) and side (bottom).

To more closely represent the blade structure, two continuous, full-length spars were added, ensuring equal spacing from the walls, and end caps were given to both the pressure and suction sides, in keeping with the definition documentation. For simplicity however, the entire blade structure material was E-Glass composite, with the material properties carried over from the QFEM Structural Blade Design Module in QBlade, as, at the time of writing, QBlade lacks the ability to incorporate orthotropic materials, and modern composite layups can produce near isotropic material properties. The material properties of the E-Glass composite are detailed in Table 1.

Table 1. E-Glass material properties.

Material Property	Value	Units
Elastic Modulus	7.30×10^{10}	Nm^{-2}
Poisson's Ratio	2.00×10^{-1}	-
Shear Modulus	3.00×10^9	Nm^{-2}
Mass Density	2.90×10^3	kgm^{-3}
Tensile Strength	1.24×10^8	Nm^{-2}
Yield Strength	4.20×10^8	Nm^{-2}

A cylindrical shaft with shaft thickness, bearing widths, and distances between each bearing and the blade mounting position, all as defined in the definition document [21], was implemented; however, diverging with the documentation, the shaft was extended forward, replacing the hub so that the blades were affixed directly to the shaft, and rearwards in observance of St. Venant's Principle, such that the stresses experienced at the generator joint area are not significantly impacted by the specific nature of the 'fixed' constraint [29], applied to the end face of the shaft, preventing local translation or deformation. The differences between the simplified model and the model defined in [21] are pictured in Figure 10.

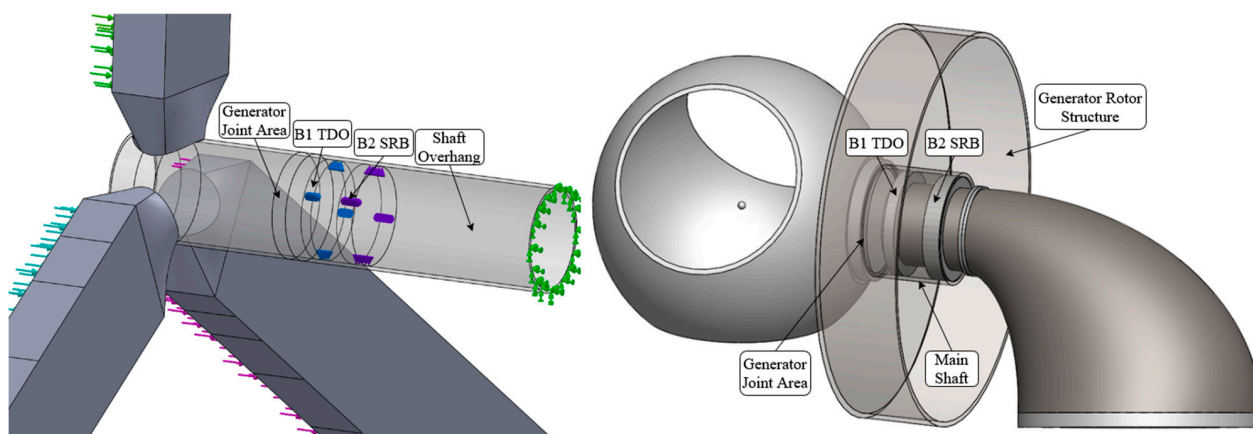


Figure 10. Comparison between simplified drivetrain (left) and original drivetrain (right).

As the specific material of the shaft is not specified in the documentation material, and in concurrence with previous work, the shaft is comprised of Carbon steel SA216 (Type WWC), with material properties as defined in Table 2.

Table 2. Carbon steel SA216 (Type WWC) material properties.

Material Property	Value	Units
Elastic Modulus	2.03×10^{11}	Nm^{-2}
Poisson's Ratio	3.00×10^{-1}	-
Shear Modulus	7.82×10^{10}	Nm^{-2}
Mass Density	7.825×10^3	kgm^{-3}
Tensile Strength	4.48×10^8	Nm^{-2}
Yield Strength	2.34×10^8	Nm^{-2}

Though the bearings were not modelled with CAD, SolidWorks Simulation allows for their effect on the structure to be accounted for through the Bearing Support Fixture function. The 'Rigid' setting assumes that no deformation or translation occurs on the surface of the bearing and requires no input, whilst 'Flexible' allows for the deformation of the bearing's face and axial displacement and requires the input of lateral (radial) and axial stiffness values. The effects of both 'Rigid' and 'Flexible' bearings were included in the structural analysis, and bearing torsional stiffness, which defines the resistance of the bearing to rotating in its seat (angular displacement) during operation, was omitted. The IEA-15MW-RWT has two main bearings that support and transmit the entire weight of the turbine's blades, hub and generator rotor and hub loads to the tower. Bearing 1 (B1_TDO) is a fixed, upwind, tapered double outer (TDO) configuration bearing with a total width of 300 mm and is assumed to carry all axial (thrust) loads and moments, whilst Bearing 2 (B2_SRB) is a floating, downwind spherical roller bearing (SRB) with a width of 470 mm. Both the blades and shaft were divided into sections using the split line feature, to accommodate the application of proportioned loads and bearings, respectively. The dimensions of the simplified drivetrain are presented below, in Table 3, and the full assembly is pictured in Figure 11b,c.

Table 3. Simplified drivetrain assembly dimensions.

Blade Property	Value	Shaft Property	Value
Length	117 m	Length	13.075 m
Depth	1628 mm	Shaft outer diameter	3000 mm
Width	4050 mm	Shaft inner diameter	2800 mm
Shell thickness	23.61 mm	Bearing outer diameter	2800 mm
Spar width	25 mm	Bearing inner diameter	2200 mm
Spar cap thickness	10 mm	B1_TDO width	300 mm
Spar centroid distance to inside wall	1334.26 mm	B1_TDO distance to rotor inner face	433.5 mm
Spar cap width	2700 mm	B2_SRB width	470 mm
Blade root distance to shaft	3000 mm	B2_SRB distance to rotor inner face	1548.5 mm
Blade mounting disc diameter	2000 mm	Shaft overhang length from B2_SRB	7565.32 mm

To verify the blade structure, the aerodynamic loads obtained under 'Rated' wind-speeds from the final timestep were applied to a single blade, and the deflection was compared against values produced in QBlade, whilst the impact of blade structure parameter changes was analysed by reducing component thicknesses (Table 4) and several simulations of the full assembly were repeated.

As each loading condition requires the application of 120 individual blade loads, 20 normal and 20 tangential loads per blade, SolidWorks' Load Case Manager was used to automate load application, and the sequential running of multiple loading scenarios.

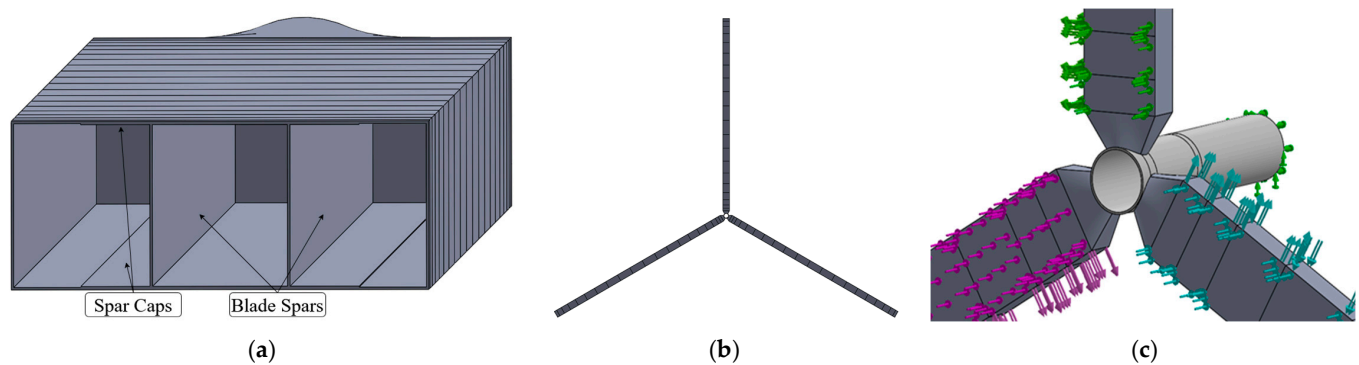


Figure 11. (a) Blade end view, (b) assembly front view and (c) assembly with applied constraints and loads.

Table 4. Reduced blade component thicknesses.

Blade Property	Original Values	Reduced Values
Length	117 m	117 m
Depth	1628 mm	1628 mm
Width	4050 mm	4050 mm
Shell thickness: top and bottom	23.61 mm	23.61
Shell thickness: side walls	23.61 mm	17.71 mm
Spar width	25 mm	12.5 mm
Spar cap thickness	10 mm	8 mm

It should be noted that although azimuth, the angular position of each blade through its rotation, affects the total blade load, its inclusion was neglected from the structural simulation, as, in order to isolate the aerodynamic loads, gravity was not included in the structural simulation of the simplified drivetrain. Gravity is, however, accounted for in the subsequent structural analysis of the PMDD rotor.

2.4. Bearing Stiffness Calculations

Whilst in reality, bearing stiffness varies as loading conditions change, this can be complicated to calculate and not feasibly integrated into the SolidWorks Simulation at present. As no values for constant axial and radial bearing stiffnesses of the IEA-15ME-RWT bearings could be found in the literature, nor could values of comparably sized bearings be easily found due to the scale of the IEA-15MW-RWT, constant stiffness values were instead calculated for each bearing. Initially, Equations (3) and (4), located in Section 2.6.2, were used to estimate the axial and radial bearing stiffnesses, respectively, by treating each bearing as a cylindrical tube of the same diameter and thickness as defined in [21]. Both bearings were assumed to be stainless steel in composition with effective lengths 75% of their overall widths. However, applying this methodology to other bearings in the literature [30–32] produced highly differing results from their known stiffness values and so the methodology was revised.

Firstly, blueprints for both bearings were drawn according to the dimensions listed in the definition documentation, and guided by examples of similar, large-scale SRB and TDO bearings in the SKF® product catalogue [33]. The resulting bearing dimensions are listed in Table 5. These blueprints, shown in Appendix A, Figures A1–A4, allowed for better informed assumptions to be made in the calculation of stiffness values for each bearing.

To find the element contact angle of the TDO bearing, the relationships between contact angle and the physical dimensions of other large TDO bearings in the SKF® catalogue were evaluated, and after finding that the bore diameter had a strong correlation (0.987) with

contact angle, the bore diameter of the IEA-15MW-RWT's bearings was used to obtain a contact angle of 23° .

Table 5. Bearing dimensions.

		³ Bore Diameter [mm]	³ Outside Diameter [mm]	² Raceway Thickness [mm]	^{1,3} Raceway Width [mm]	² Roller Lengths [mm]	¹ Roller Diam. [mm]	¹ Contact Angle [$^\circ$]	² Roller Azimuth [$^\circ$]	² Number of Rollers [-]
TDO	Outer	2200	2800	65	230.05 ⁽¹⁾	92.5	41	23	2.09	172
	Inner	-	-	130	300 ⁽³⁾	-	40	-	-	-
SRB	Outer	2200	2800	94.5	470 ⁽³⁾	176.25	150	15.5	7.2	50
	Inner	-	-	78.75	470 ⁽³⁾	-	-	-	-	-

Values obtained through: ¹ extrapolation, ² drawings and ³ directly from the GitHub repository [21].

This process was repeated to find the diameters of the B1_TDO's shaft and housing abutments, and the B2_SRB's inner shoulder diameter and outer recess diameters.

To calculate bearing stiffness, each bearing was split into three constituent parts, inner ring, roller elements and outer ring, all assumed to be composed of stainless steel ($E = 195\text{GPa}$, $G = 77.2\text{GPa}$), so that the stiffnesses of each component could be calculated individually, and summed to produce the total bearing stiffness, according to series spring theory (Equation (5)). The total system stiffness can then be obtained according to parallel spring theory, using Equation (6).

2.4.1. Raceway Stiffness

To calculate raceway stiffness, each raceway was treated as a cylinder, with their widths and thicknesses taken as their average according to their technical drawings, presented in Table 5, and their axial and radial stiffness calculated using Equations (3) and (4), using area and area moment of inertia as calculated by Equations (7) and (8), respectively.

Applying the values presented in Table 5 to the above mentioned equations produced axial stiffness values of $3.92 \times 10^{11} \text{ Nm}^{-1}$ and $4.73 \times 10^{11} \text{ Nm}^{-1}$ for the inner and outer raceways of B1_TDO, respectively, and $2.34 \times 10^{11} \text{ Nm}^{-1}$ and $3.33 \times 10^{11} \text{ Nm}^{-1}$ for B2_SRB's inner and outer raceways, respectively. The radial stiffness of B1_TDO's inner and outer raceways were found to be $7.49 \times 10^{13} \text{ Nm}^{-1}$ and $1.34 \times 10^{14} \text{ Nm}^{-1}$, respectively, whilst B2_SRB's inner and outer raceways were found to have radial stiffness values of $1.10 \times 10^{13} \text{ Nm}^{-1}$ and $2.21 \times 10^{13} \text{ Nm}^{-1}$, respectively.

2.4.2. Stiffness of Rolling Elements

To estimate the stiffness of the roller elements for the SRB and TRB, Equations (9) and (10) [34] were used, respectively, ensuring all bearing dimensions and forces were converted to imperial.

Roller element dimensions such as diameter (D), the number of roller elements (Z), length (L) and contact angle (α) were obtained from the technical drawings, whilst external radial force (F) was obtained through the following process.

The total radial force due to component masses was taken from the IEA-15MW-RWT definition document, and found to be 530,713 kg, producing 5204.72 kN. This was assumed to be transferred to the tower in an even split through the TDO and SRB bearings. A structural simulation as described in Section 2.3 was then run with bearings set to 'Rigid', and the reaction at each bearing obtained, with B1_TDO experiencing a reaction force of -792.29 kN and B2_SRB experiencing a reaction force of 6166.7 kN. This produced total forces on Bearings 1 and 2 of 1810 kN and 8769 kN, respectively. Applying these

values to Equations (9) and (10) gave radial stiffness values of $1.02 \times 10^{11} \text{ Nm}^{-1}$ and $3.97 \times 10^{10} \text{ Nm}^{-1}$ for the rolling elements of Bearings 1 and 2, respectively.

Again, using examples of bearings in the SKF® product catalogue, the ratio between the radial and axial stiffnesses of the TDO rolling elements was found to be strongly correlated (0.989) with element contact angle, which was subsequently used to extrapolate a ratio of 0.6, giving the B1_TDO a rolling element axial stiffness of $6.12 \times 10^{10} \text{ Nm}^{-1}$. As only Bearing 1 supports axial loading, Bearing 2's axial stiffness was omitted. Using Equation (11), the total bearing stiffnesses can be obtained.

As presented in Table 6, this finds that Bearings 1 (TDO) and 2 (SRB) have a total radial stiffnesses of $1.02 \times 10^{11} \text{ Nm}^{-1}$ and $3.95 \times 10^{11} \text{ Nm}^{-1}$, respectively, and that B1_TDO has a total axial stiffness of $4.76 \times 10^{10} \text{ Nm}^{-1}$. The combined radial stiffness can then be obtained using Equation (12), finding the total system radial stiffness of $1.41 \times 10^{11} \text{ Nm}^{-1}$, some 3.7 times greater than that of the 5 MW device presented in [30].

Table 6. Bearing stiffnesses.

Component	Bearing 1_TDO		Bearing 2_SRB
	Axial Stiffness [Nm^{-1}]	Radial Stiffness [Nm^{-1}]	Radial Stiffness [Nm^{-1}]
Inner raceway	3.918×10^{11}	7.485×10^{13}	1.101×10^{13}
Rolling element	6.124×10^{10}	1.021×10^{11}	3.968×10^{10}
Outer raceway	4.734×10^{11}	1.339×10^{13}	2.211×10^{13}
Bearing total	4.763×10^{10}	1.018×10^{11}	3.946×10^{10}
System total	4.763×10^{10}	1.413×10^{11}	

2.4.3. Validation of Bearing Stiffnesses

In validating bearing stiffnesses, the working stiffness of the bearing mounting surface is obtained to serve as a minimum requirement for the bearings to meet, using the process described in Section 2.6.3.

This found that the minimum required stiffness at Bearings 1 and 2 was found to be $2.097 \times 10^{10} \text{ Nm}^{-1}$ and $3.286 \times 10^{10} \text{ Nm}^{-1}$, respectively. The stiffness for the main bearings of the IEA-15MW-RWT, obtained using the method devised in this paper, was found to be 386% and 20% larger than the minimum requirement for Bearings 1 and 2, respectively.

2.5. Parametric Optimisation of the Generator Rotor

The parametric optimisation of the rotor structure of the IEA-15MW-RWT was carried out within the ANSYS Workbench (version 2021 R2), using Static Structural and Response Surface Optimisation modules. The outer rotor—comprising a disk-supported, end-mounted cylinder, that serves as host to the permanent magnets—was imported with a direct link from SolidWorks using the ANSYS CAD Configuration Manager. The rotor has an airgap diameter of 10.53 m, a stack length of 2.17 m and a mounting cylinder diameter of 3 m.

A fixed support was first applied to the inner face of the rotor disk, which connects to the simplified drivetrain; a torque (τ_f) of 21 MNm was then applied uniformly and normally to the inner cylinder surface. Centrifugal forces were accounted for with a global rotational velocity (ω) of 0.79 rads^{-1} . The in-plane component of standard earth gravity (g) was applied (9.76 ms^{-2}), accounting for the rotor's 6° upwards tilt. A uniform fixed mass of 24,289 kg was applied to the inner surface of the cylinder, to represent the mass of permanent magnets. This work assumes that the carbon steel SA216 (Type WWC) material used in the drivetrain is likewise used for the rotor, and that the carbon steel can fulfil the role of the back iron. The final load imposed on the generator was a static, radial

compression load arising from magnetic attraction, applied to the inner cylinder surface, representing the normal component of Maxwell's electromagnetic stress (σ_{PM}).

The deformation of the rotor structure that arises from Maxwell's stresses can take a number of forms, as shown in Figure 12, where (a) Mode 0 is a radial contraction of the rotor into the airgap, (b) Mode 1 is a relative displacement of the rotor to and from the stator and (c) Mode 2 is an elliptical distortion of the rotor surface, whilst (d) Modes 3 and upwards have an increasing number of rippled distortions of the airgap surface. The stator is pictured in grey, the undeformed rotor in light blue and the deformed rotor in dark blue, with arrows denoting the localised deflection. Equation (15) in Section 2.6.4 can be used to calculate the sinusoidal variance of local Maxwell's electromagnetic stress for Modes 1 and upwards.

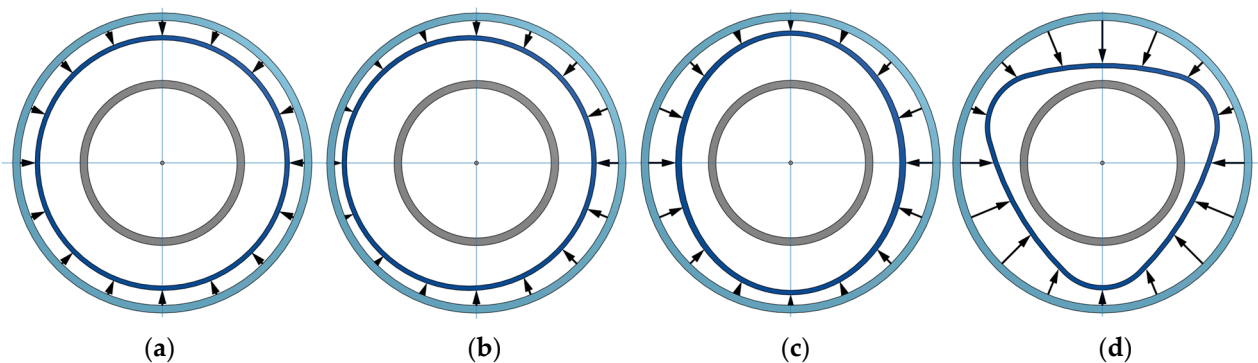


Figure 12. Modal deformation of an outer rotor: (a) Mode 0, (b) Mode 1, (c) Mode 2 and (d) Mode 3.

As shown in Figure 13, a uniform load of -447.1 kPa was applied to the cylinder at Mode 0, whilst Modes 1+ were found to produce sinusoidal loads with minima and maxima of -461.2 kPa and -432.9 kPa, respectively, about a mean load of -447.1 kPa.

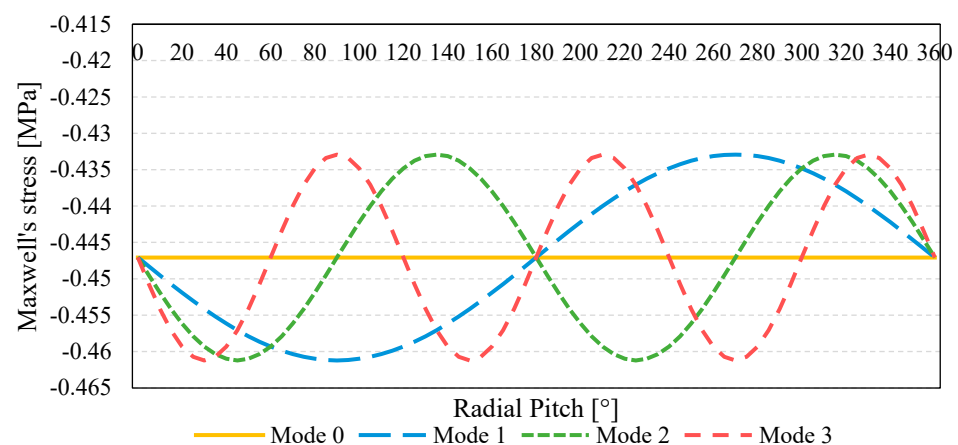


Figure 13. Modal loading on the PMDD generator structure.

Previous work has indicated Mode 1 results in the greatest airgap deformations; however, an examination of the electromagnetic and mechanical loading on the rotor determined that, as the mass of the magnets and cylinder produces a moment around the X-axis as shown in Figure 14a,b, electromagnetic stresses which align vertically are the most dangerous by accentuating gravitational loading, and so the structure was optimised under Mode 2, using a cylindrical coordinate system (Figure 14c) to apply the waveform in 5° increments, and each structure was further examined under Mode 0 loading.

The response surface optimisation tool was used to map the relationship between the component thicknesses and their structural response to the applied loading conditions by first examining 12 initial samples with disk thicknesses varying between 200 and 600 mm,

and cylinder thicknesses between 100 and 350 mm, using the Latin hypercube sampling method. The multi-objective genetic algorithm function was then used to produce three candidates for each deformation limit, based on the generated response surface. A 'seek' objective and constraint was used to ensure a proximity of within 0.005 mm below the target deformation limit, and an objective to minimise mass was set with no constraint applied. The deformation was measured from the inner cylinder face, and the candidate with the lowest mass to achieve the deformation limit to within 1% was carried forward.

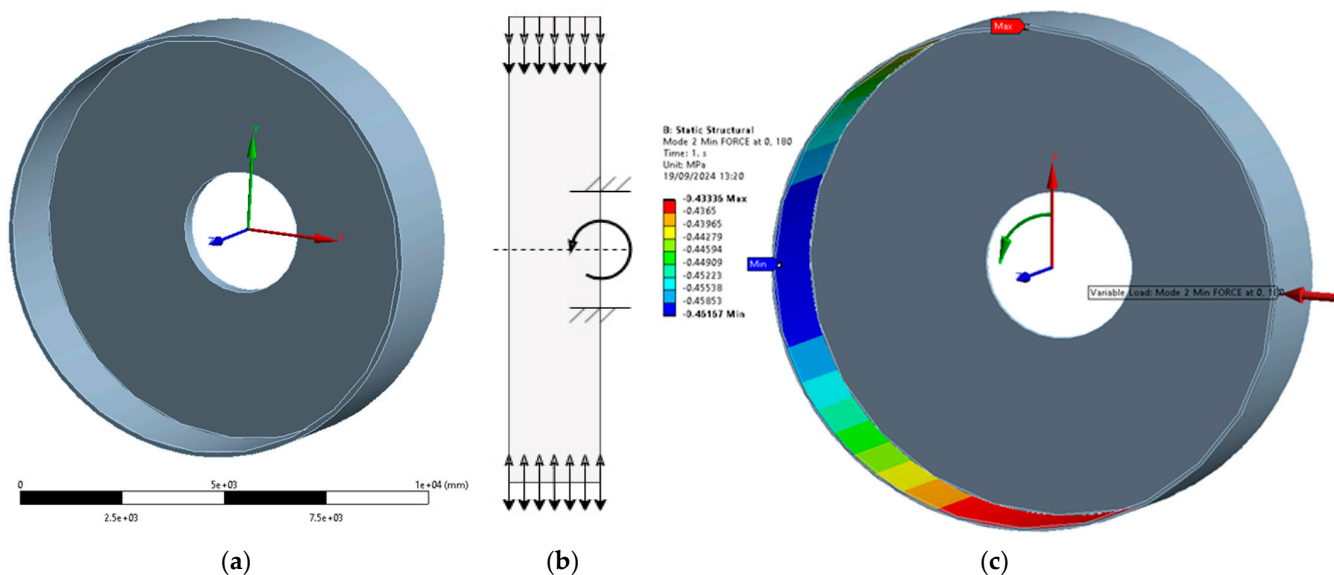


Figure 14. (a) The IEA-15MW-RWT generator rotor with Cartesian coordinate system, (b) rotor side view with gravity and Maxwell's stress interaction and (c) rotor with Mode 2 loading applied and cylindrical coordinate system.

Where all three candidates diverged from their predicted deformation or stress values by more than 1% when verified, these candidates were then inserted as refinement points by which to improve the accuracy of the response surface at that deformation limit, and the optimisation was run again.

2.6. Governing Equations

2.6.1. Generator Power

$$P = T * \omega \quad (1)$$

$$T = 2\pi R^2 \sigma l \quad (2)$$

where P is power (W), T is torque (Nm), ω represents rotational velocity (rad/s), R is the radius of the generator (m), σ is the shear stress (Pa) and l is stack (magnet) length (m).

2.6.2. Bearing Stiffness Calculation

$$K_{axial} = \frac{E * A}{L} \quad (3)$$

$$K_{radial} = \frac{E * I}{L} \quad (4)$$

where K_{axial} and K_{radial} are the axial and radial raceway stiffness, respectively (Nm⁻¹), E is the elastic modulus (Pa), A is area (m²), L is length (m) and I represents area moment of inertia.

$$K_{series_{Tot}} = \frac{1}{\frac{1}{K_1} + \frac{1}{K_2} + \frac{1}{K_3}} \quad (5)$$

$$K_{parallel_{Tot}} = K_1 + K_2 \quad (6)$$

where $K_{series_{Tot}}$ is the total series stiffness according to series spring theory, K_1 to K_3 are the stiffnesses of individual elements and $K_{parallel_{Tot}}$ is the total parallel stiffness according to parallel spring theory.

$$A = \pi * (r_o^2 - r_i^2) \quad (7)$$

$$I = \frac{\pi}{4} * (D_o^4 - D_i^4) \quad (8)$$

where r_o is the outside radius of the raceway (m), r_i is inside radius of the raceway (m), D_o is the outside diameter of the raceway (m) and D_i is insider diameter raceway (m).

$$K_{SRE} = 0.0921E06 * \sqrt[4]{FL^2Z^3\cos^7\alpha} \quad (9)$$

$$K_{TRE} = 0.300E06 * F^{0.1}Z^{0.9}L^{0.8}\cos^{1.9}\alpha \quad (10)$$

where K_{SRE} and K_{TRE} are the radial stiffness (Lbf/in) of spherical and tapered roller elements, respectively, F is the external radial force (Lbf), D is the roller diameter (in), Z and L are the number of roller elements and their effective length (in), respectively, and α is their contact angle (rad).

$$K_{bearing_{Tot}} = \frac{1}{\frac{1}{K_{Inner\ raceway}} + \frac{1}{K_{Roller\ element}} + \frac{1}{K_{Outer\ raceway}}} \quad (11)$$

where $K_{bearing_{Tot}}$ is the total bearing stiffness according to series spring theory, and K_1 to K_3 are the stiffnesses of the inner raceway, rolling elements and outer raceway, respectively.

$$K_{system_{Tot}} = K_{B1} + K_{B2} \quad (12)$$

where $K_{system_{Tot}}$ is the total combined radial stiffness of Bearings 1 (K_{B1}) and 2 (K_{B2}).

2.6.3. Bearing Stiffness Validation

$$E = \sigma / \varepsilon \quad (13)$$

$$\varepsilon = \Delta l / L \quad (14)$$

By combining the definition of Young's modulus of elasticity (Equation (13)) with the definition of strain (Equation (14)), where L and Δl are the thickness and change in shaft thickness, respectively (m), we derive the expression for axial deformation in Equation (15).

$$\Delta l = \frac{\sigma}{E} * L \quad (15)$$

$$F = \sigma * A \quad (16)$$

Then, substituting the force F , obtained from Equation (16), where F is obtained at the point of maximum stress (Nm^{-1}) and A is the corresponding approximate area of maximum stress (m^2), and the deformation obtained from Equation (15) into the expression for stiffness (Equation (17)),

$$K = F / \Delta l \quad (17)$$

We obtain spring stiffness in Equation (18):

$$K = \frac{A * E}{L} \quad (18)$$

2.6.4. Modal Loading

$$\sigma_{\theta PM} = \frac{\hat{B}^2}{2\mu_0} \left[1 + \frac{2\delta_{\Delta}}{g + \frac{h_m}{\mu_r} - \bar{\delta}} \right] \quad (19)$$

where $\sigma_{\theta PM}$ is the local stress (Pa) at pitch θ for a PMDD machine, \hat{B} is the peak airgap magnetic flux density (Wb/m²), μ_0 is the permeability of free space (H/m), δ_{Δ} is the local deflection under each mode, g is the nominal airgap clearance, h_m is the magnet height (m), μ_r is the relative permeability of air and $\bar{\delta}$ is the mean radial deflection (m).

3. Results

3.1. Aero-Servo-Elastic Simulation Results

In total, the normal and tangential aerodynamic loading results of six scenarios were obtained to investigate the structural response of the drivetrain to aerodynamic loads at expected wind conditions, with ‘Rated’ and ‘High’ windspeeds, and ‘Flexible’ and ‘Rigid’ bearing settings used in each of the following:

1. Final simulation timestep;
2. Highest total normal load across rotor;
3. Highest total tangential load across rotor;
4. Highest combined normal and tangential load across rotor;
5. Greatest normal rotor load imbalance;
6. Greatest tangential rotor load imbalance.

The results taken from the final timestep presented a marked, unexpected difference between the results of the ‘Rated’ and ‘High’ settings, as the total normal blade load is 96% greater at ‘Rated’ than at ‘High’, and the total tangential blade load is 38% lower than at ‘High’ windspeeds. This change in blade load profile we attribute to the use of collective blade pitch in order to reduce the aerodynamic torque and maintain the maximum rotor speed in above rated wind speeds; as shown in Figure 15, significantly higher levels of blade pitch were required throughout under ‘High’ windspeeds.

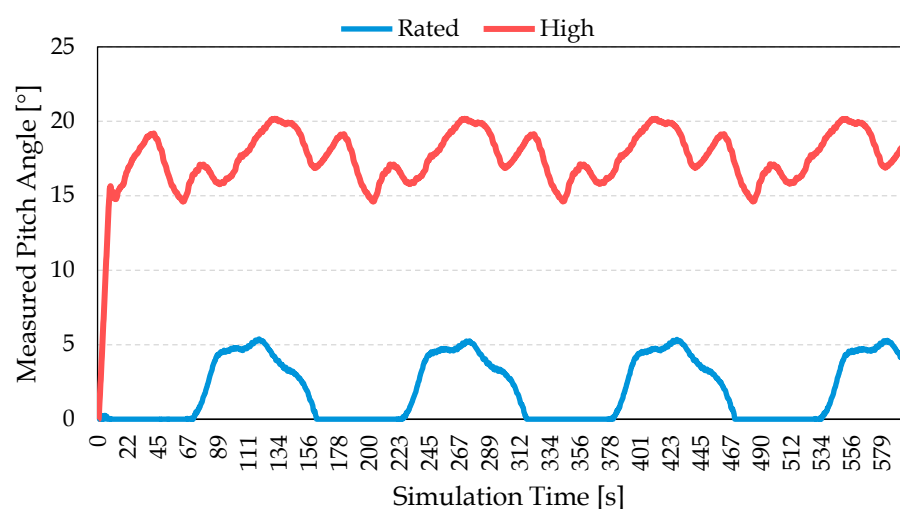


Figure 15. Blade pitch angle at ‘Rated’ and ‘High’ speeds.

This is likewise reflected in Figures 16 and 17, which display the total normal and tangential load, respectively, on blade 1 throughout the simulation.

As shown in Figure 16, the average total normal load throughout the simulation at ‘High’ conditions is 44% lower than at ‘Rated’ windspeeds, though tangential loading is 77% greater on blade 1 at ‘High’ conditions than at ‘Rated’ (Figure 17). Additionally, both normal and tangential loads exhibit significantly more variability at ‘High’ conditions.

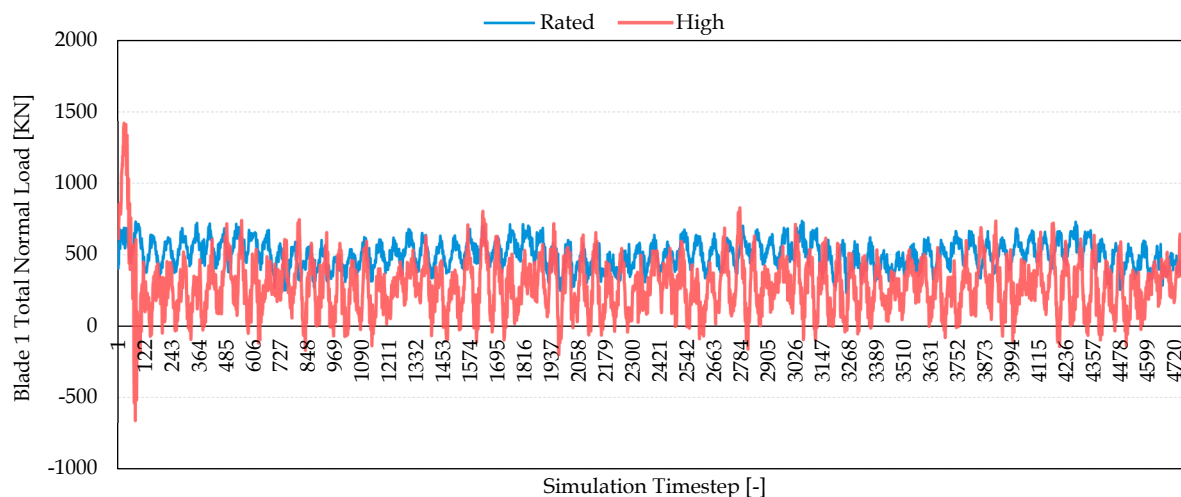


Figure 16. Total normal load on blade 1 at ‘Rated’ and ‘High’ conditions.

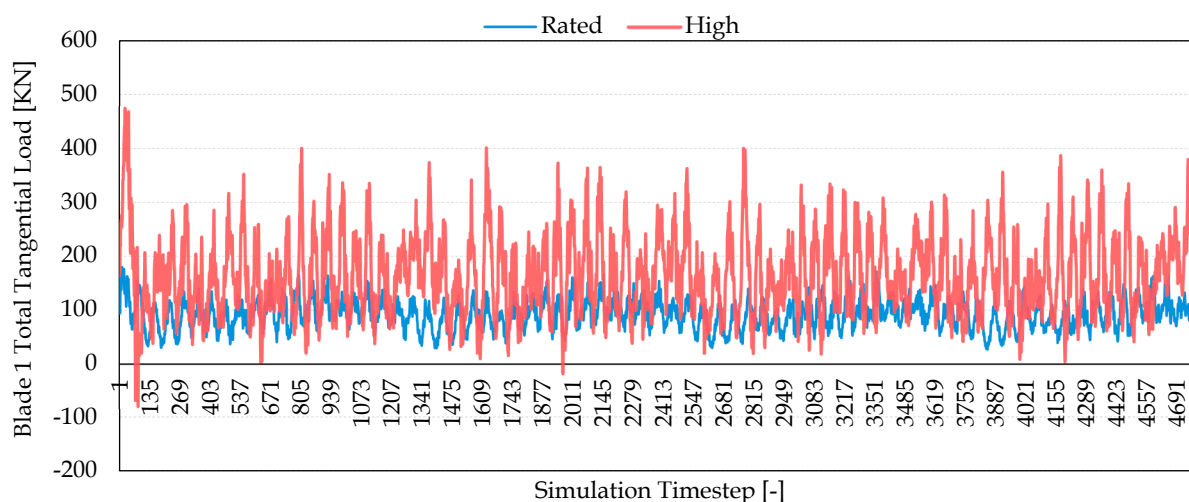


Figure 17. Total tangential load on blade 1 at ‘Rated’ and ‘High’ conditions.

The highest normal and tangential blade loads across the rotor were experienced at 4.75 and 1.5 s, respectively, at ‘Rated’ conditions, whilst their combination occurred at 1.75 s, and at ‘High’ windspeeds, both occurred at 5.25 s. That the highest levels of blade loading were all recorded within the first 1% of the simulation indicates that loading is heightened as the control system start-up procedure lags the change to incoming flow, an effect which is exacerbated at above rated wind speeds; this can be seen in Figure 17.

Contrary to the maximum blade loading occurrences, the largest imbalance in normal and tangential loading across the rotor plane occurred 249 s and 559.63 s, respectively, under ‘Rated’ conditions, and at 487.25 s and 101.25 s, respectively, at ‘High’ windspeeds.

The timesteps that represent the largest normal load imbalance across the rotor plane under ‘Rated’ wind speeds, and the highest tangential imbalance at ‘High’ wind speeds are presented in Figures 18 and 19, respectively.

For the visualisation of the load imbalances, Figure 18 displays tangential loading on a separate axis from the normal load, whilst Figure 19 visualises the difference in magnitude between tangential and normal loads through the same axis scales.

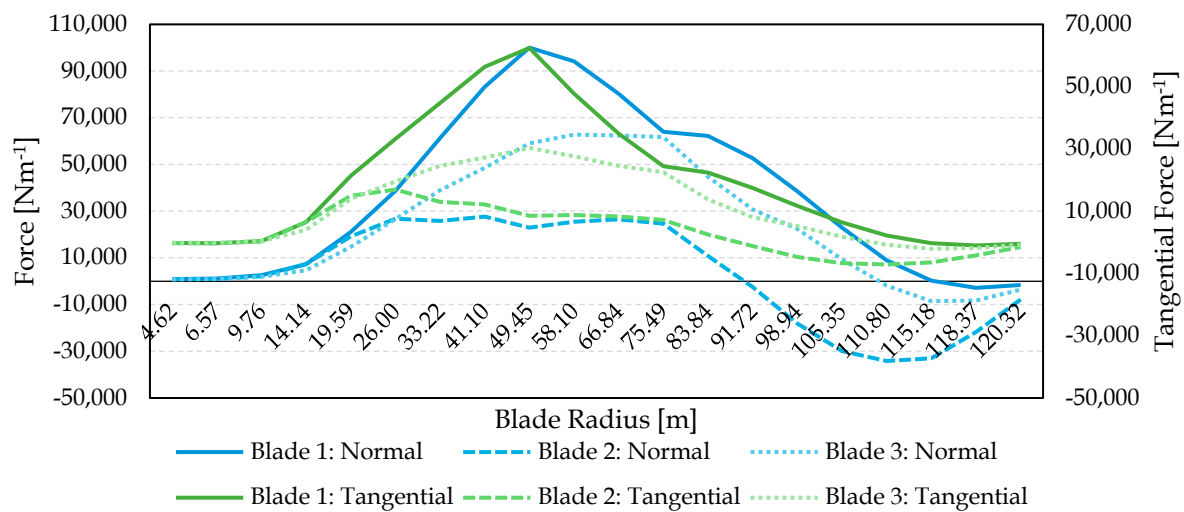


Figure 18. Distributed normal and tangential blade loads at the timestep corresponding to the greatest tangential load imbalance, 'High' conditions.

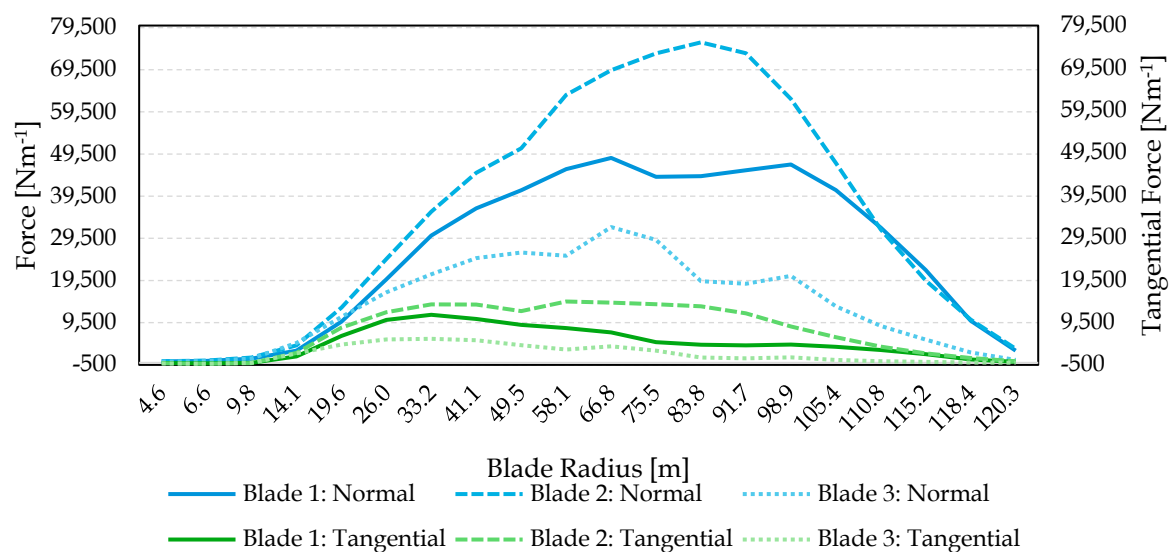


Figure 19. Distributed normal and tangential blade loads at the timestep corresponding to the greatest normal load imbalance, 'Rated' conditions.

3.1.1. Mesh Independence Study

A mesh independence study was carried out in two steps, firstly finding convergence for a single blade with maximum and minimum mesh element sizes of 375 mm and 337.85 mm, respectively. With the blade mesh obtained and implemented in a full assembly, a mesh independence of the shaft was carried out, finding convergence with a blended, curvature-based mesh with maximum and minimum element sizes of 200 and 180 mm, respectively, for the shaft. The result was a total of 583,451 nodes and 299,391 elements.

3.1.2. Load Transfer Structural Analysis

In total, this section details the results of 12 simulations designed to investigate the drivetrain's structural response to a range of wind conditions, presented in Tables 7 and 8, which contain the results of the 'Rated' and 'High' windspeed simulations, respectively.

Table 7. Results of the load transfer analysis: ‘Rated’ conditions.

Conditions	S1: Final Timestep		S2: Greatest Normal Load	S3: Greatest Tang. Load	S4: Greatest Total Combined	S5: Largest Norm. Imbalance	S6: Largest Tang. Imbalance	Units
	Norm. Only	Norm. and Tang.						
Max. Blade Displ. (Rigid)	−13.16	−13.16	−17.89	−16.78	−16.88	−12.93	−13.77	m
Max. Blade Displ. (Flex.)	−13.17	−13.16	−17.90	−16.78	−16.88	−12.94	−13.78	m
Max. Shaft Displ. (Rigid)	9.943	11.603	15.521	14.911	15.288	14.225	15.169	mm
Max. Shaft Displ. (Flex.)	9.959	11.774	15.704	15.004	15.135	14.607	15.552	mm
Max. Gen. Area Displ. (Rigid)	1.233	2.111	2.190	2.430	2.219	1.737	1.829	mm
Max. Gen. Area Displ. (Flex.)	1.311	2.172	2.254	2.488	2.256	1.858	1.937	mm
Max. Gen. Area Stress (Rigid)	63.393	77.450	89.381	94.504	90.665	88.824	94.716	MPa
Max. Gen. Area Stress (Flex.)	63.335	77.442	89.465	94.569	90.593	88.837	94.727	MPa
B1_TDO Max. Radial Stress (Flex.)	15.315	16.872	21.585	19.893	17.980	17.023	18.171	MPa
B2_SRB Max. Radial stress (Flex.)	2.874	2.907	2.652	3.053	2.212	6.604	6.414	MPa
Shaft Eccentricity (Rigid)	12.1	20.8	21.6	23.9	21.9	17.1	18.0	%
Shaft Eccentricity (Flex.)	12.9	21.4	22.2	24.5	22.2	18.3	19.1	%
New Limit (Rigid)	1.783	1.608	1.592	1.544	1.586	1.683	1.664	mm
New Limit (Flex.)	1.768	1.596	1.579	1.532	1.579	1.658	1.643	mm

Table 8. Results of the load transfer analysis: ‘High’ conditions.

Conditions	S1: Final Timestep		S4: Worst Total Combined Load	S5: Largest Normal Imbalance	S6: Largest Tangential Imbalance	Units
	Normal Only	Normal and Tang.				
Max. Blade Displacement (Rigid)	0.58	1.19	−27.49	−13.90	−9.48	m
Max. Blade Displacement (Flex.)	0.58	1.19	−27.49	−13.92	−9.48	m
Max. Shaft Displacement (Rigid)	0.310	4.053	27.763	27.705	17.942	mm
Max. Shaft Displacement (Flex.)	0.323	4.136	28.007	28.617	18.445	mm
Max. Gen. Area Displacement (Rigid)	0.050	0.811	5.649	3.595	2.449	mm
Max. Gen. Area Displacement (Flex.)	0.055	0.835	5.722	3.924	2.613	mm
Max. Gen. Area Stress (Rigid)	2.150	26.511	190.942	166.628	125.784	MPa
Max. Gen. Area Stress (Flex.)	2.151	26.512	190.948	166.643	125.801	MPa
B1_TDO Max. Radial Stress (Flex.)	0.312	3.503	36.088	37.310	21.536	MPa
B2_SRB Max. Radial Stress (Flex.)	0.237	1.274	5.036	13.048	9.798	MPa
Shaft Eccentricity (Rigid)	0.005	0.080	0.557	0.354	0.241	%
Shaft Eccentricity (Flex.)	0.005	0.082	0.564	0.387	0.257	%
New Limit (Rigid)	2.020	1.868	0.900	1.311	1.540	mm
New Limit (Flex.)	2.019	1.863	0.886	1.245	1.507	mm

In scenario 1, the higher level of normal loading present in the last timestep of the ‘Rated’ aero-servo-elastic simulation versus the ‘High’ scenario was reflected in the structural results, with stresses and displacements significantly higher across the system under ‘Rated’ conditions.

A blade deflection of 13.16 m was observed with ‘Rated’ conditions, with marginal differences in maximum blade displacement found between normal loads on their own versus the introduction of additional tangential loads (0.01%), and with ‘Rigid’ and ‘Flexible’ bearings (0.02%); notably, the former trend was sustained through all of the observed loading scenarios, indicating, as expected, that main bearing stiffness has a negligible impact on blade deformation. With ‘Flexible’ bearings, the maximum shaft displacement of 9.959 mm was obtained, an increase of 0.2%, whilst generator area displacement increased by 6.29% to 1.31 mm, and maximum generator area stress decreased by 0.1%, to 63.4 MPa. Whilst the introduction of tangential loads had a negligible effect on blade displacement, it

had a significant effect on all other parameters, increasing shaft displacements by 16.7% and 18.2%, generator area displacements by 71.2% and 65.7% and maximum generator stress by 22.2% and 22.3%, respectively for 'Rigid' and 'Flexible' bearings. Maximum stress on the mounting surface of Bearing 1 increased by 10.2% with the inclusion of tangential loads, and by 1.2% for Bearing 2.

At 'High' windspeeds, due to the negative normal loading at the blade tip under 'High' conditions, blade displacement is slightly reversed, and the lowest levels of displacement and stress across the full simplified drivetrain system are present. 'Flexible' bearings were found to increase maximum shaft and generator area displacements by 4.1% and 10.8%, to 0.2 mm and 0.06 mm, respectively, over 'Rigid' bearings; however, the inclusion of tangential loading on the results of the final timestep was significant, doubling maximum blade displacement and increasing shaft and generator area displacements by over 1200% and 1500%, to 4.05 mm and 0.81 mm, respectively, for 'Rigid' bearings and 1100% and 1400%, to 4.14 mm and 0.84 mm, respectively, for 'Flexible' bearings. Maximum generator stress was found to increase by over 1100% to 26.5 MPa with the inclusion of tangential blade loads, though a marginal difference between 'Rigid' and 'Flexible' bearings was found. Finally, maximum radial stress at the bearings was found to increase by around 1000% and 440%, to 3.5 MPa and 1.3 MPa, for Bearings 1 and 2, respectively, with the inclusion of tangential loading.

For scenario 2, corresponding to the timestep with the highest total normal load across the rotor, it can be observed that as expected, at 'Rated' conditions, the higher normal load produced a maximum blade deflection of 17.9 m, 6.6% larger than the timestep with the highest tangential load (scenario 3). Maximum shaft displacement was likewise higher, though to a lesser extent, at 4.1% and 4.7% with 'Rigid' and 'Flexible' bearings, respectively. However, a different trend was seen at the generator area, with displacements of 2.43 mm and 2.49 mm under scenario 3, some 11% and 10.4% higher displacement than scenario 2 with 'Rigid' and 'Flexible' bearings, respectively, and maximum stress was likewise higher by 5.7%. Stress at the surfaces of Bearing 1 was 8.5% higher under the highest normal load burden than under the highest tangential load, whilst Bearing 2 saw a 13.1% decrease. The timestep corresponding to the highest combined normal and tangential load burden (scenario 4) at 'Rated' conditions found marginally higher blade and shaft deflections than the highest tangential load burden; however, maximum stress and displacement at the generator area was found to be 4.1% and 8.7% lower, respectively, with 'Rigid' bearings, and 4.2% and 9.3% lower with 'Flexible' bearings.

At 'High' windspeeds, scenarios 2 and 3 were found to coincide at the same timestep, therefore corresponding to scenario 4. The highest level of blade deflection was found at this timestep, at 27.5 m, and exceeded the worst-case out-of-place blade deflection of 22.8 m specified in the definition documentation [21]; however, considering the 4m tip pre-bend of the IEA-15MW-RWT is not present in the simplified structural model devised in this work, and that the IEA-15MW turbine has an unloaded blade tip-to-tower clearance of 30 m, this can be considered in-line with expectations. Maximum shaft displacements of 27.7 mm and 28.1 mm were obtained from 'Rigid' and 'Flexible' bearings settings, respectively, 82% and 87% higher than the same scenario at 'Rated' windspeeds. Maximum generator area stresses of 190.9 MPa were obtained under 'Flexible' and 'Rigid' settings, 111% higher than those obtained under 'Rated' conditions. The maximum generator area displacement was likewise considerably higher, 155% and 154%, than the same scenario for 'Rated' windspeeds for 'Rigid' and 'Flexible' bearings, respectively. Across all scenarios, the mounting surface of Bearing 1 was found to undergo significantly higher levels of radial stress than Bearing 2, as a result of being upwind of Bearing 2 and closer to the application

of aerodynamic loads on the main shaft, and this case is no different, with a maximum radial stress of 36.1 MPa at Bearing 1 and 5.0 MPa at Bearing 2.

In Scenario 6, the timestep with the largest normal load imbalance across the rotor plane found a maximum blade displacement of 12.9 m at ‘Rated’ conditions, and 13.9 m at ‘High’, giving rise to maximum shaft displacements of 14.6 mm at ‘Rated’ with ‘Flexible’ bearings and 28.6 mm at ‘High’ with ‘Flexible’ bearings. Generator area displacements of 1.74 mm and 1.86 mm at ‘Rated’ conditions were roughly doubled under ‘High’ conditions, at 3.60 mm and 3.92 mm with ‘Rigid’ and ‘Flexible’ bearing settings, respectively. Likewise, generator area Von Mises stress was nearly doubled from ‘Rated’ to ‘High’ wind conditions, though consistent between bearing settings, with 88.8 MPa at ‘Rated’, and 166.63 MPa at ‘High’ windspeeds. The maximum stress on the mounting surfaces of Bearings 1 and 2 increased by 119% and 98%, respectively, with the increase in windspeed from ‘Rated’ to ‘High’.

In the final scenario (7), the timestep with the highest tangential load imbalance across the rotor plane, at ‘Rated’ conditions, a 6.5% greater maximum blade displacement was observed than in Scenario 6, at 13.8 m, as higher levels of normal loading are present than in Scenario 6. Accordingly, maximum shaft and generator area displacements are likewise elevated above Scenario 6, with shaft displacements at 15.17 mm and 15.55 mm with ‘Rigid’ and ‘Flexible’ bearings, respectively, and generator area displacements at 1.83 mm and 1.94 mm, respectively. Stress at the generator area is likewise higher, at 94.72 MPa with ‘Rigid’ bearings, and whilst radial stress at the surface of Bearing 1 was also found to increase by a similar amount, Bearing 2 was found to experience 3% lower radial stress than under Scenario 1.

At ‘High’ wind speeds, Scenario 7 sees lower normal forces than in Scenario 6, as is reflected by the reduction of maximum blade, shaft and generator area displacements by between 31.8% and 35.5% against those of Scenario 6. Stresses are likewise reduced, with maximum Von Mises stress at the generator area 24.5% smaller, whilst Bearings 1 and 2 were 42.3% and 24.9% lower, respectively. Both Scenarios 6 and 7 found that at ‘High’ wind speeds, at least one blade had a reversed maximum blade deflection, with the normal load imbalance scenario producing a maximum negative blade displacement of 5.5 m with ‘Flexible’ bearings, and 3.7 m under the tangential imbalance scenario. To further evaluate how the addition of tangential loading affects drivetrain stability, four additional simulations were carried out, which pertain to Scenarios 2 and 5, with ‘Flexible’ bearings, and no tangential loads, as presented in Tables 9 and 10 for ‘Rated’ and ‘High’, respectively.

Table 9. Introduction of tangential loads at ‘Rated’ conditions with ‘Flexible’ bearings.

Conditions	S1: Final Timestep		S2: Greatest Total Normal Load		S5: Largest Normal Load Imbalance		Units
	Normal Only	Normal and Tang.	Normal Only	Normal and Tang.	Normal Only	Normal and Tang.	
Max. Blade Displacement	−13.17	−13.16	−17.88	−17.90	−12.95	−12.94	m
Max. Shaft Displacement	9.959	11.774	13.507	15.704	13.525	14.607	mm
Max. Gen. Area Displacement	1.311	2.172	1.443	2.254	1.799	1.858	mm
Max. Von Mises Gen. Area stress	63.34	77.44	75.11	89.46	75.93	88.84	MPa
B1_TDO Max. Radial Stress	15.32	16.87	19.24	21.59	19.44	17.02	MPa
B2_SRB Max. Radial stress	2.87	2.91	2.68	2.65	6.50	6.60	MPa
Shaft Eccentricity	12.9	21.4	14.2	22.2	17.7	18.3	%
New Limit	1.768	1.596	1.741	1.579	1.670	1.658	mm

This finds that with the exception of Scenario 1 under ‘High’ conditions, the inclusion of tangential loading had no considerable impact on maximum blade displacement; however, the presence of tangential loading does have an appreciable effect on maximum

shaft and generator area displacements and stresses. Under Scenario 2, maximum generator area displacement is increased by 56.2% by the inclusion of tangential loading at ‘Rated’ conditions, and 114.8% at ‘High’ conditions. This effect is minimal under Scenario 5 with maximum generator area displacement increased by just 3.3% at ‘Rated’ windspeeds; however, at ‘High’ conditions, generator area displacement is increased by 41.2%.

Table 10. Introduction of tangential loads at ‘High’ conditions with ‘Flexible’ bearings.

Conditions	S1: Final Timestep		S2(4): Greatest Total Normal (Combined) Load		S5: Largest Normal Load Imbalance		Units
	Normal Only	Normal and Tang.	Normal Only	Normal and Tang.	Normal Only	Normal and Tang.	
Max. Blade Displacement	0.58	1.19	−27.46	−27.49	−13.87	−13.92	m
Max. Shaft Displacement	0.323	4.136	21.865	28.007	21.449	28.617	mm
Max. Gen. Area Displacement	0.055	0.835	2.664	5.722	2.779	3.924	mm
Max. Von Mises Gen. Area Stress	2.15	26.51	133.18	190.95	110.46	166.64	MPa
B1_TDO Max. Radial Stress	0.31	3.50	31.80	36.09	26.58	37.31	MPa
B2_SRB Max. Radial Stress	0.24	1.27	4.85	5.04	13.20	13.05	MPa
Shaft Eccentricity	0.5	8.2	26.2	56.4	27.4	38.7	%
New Limit	2.019	1.863	1.497	0.886	1.474	1.245	mm

To examine the effect of blade simplification and the assumptions made to produce the blades, and consequently provide further verification of the stress and displacements obtained at the generator area, Scenarios 1–4 are repeated with reduced blade component thicknesses, as defined in Table 4.

Under all loading scenarios, the reduced blade component thicknesses produced an increased blade deflection of between 10.0% and 10.1%, considering both ‘Rigid’ and ‘Flexible’ bearing settings and ‘Rated’ and ‘High’ windspeeds, the effect on all other measures was minimal however, with the greatest change being a decrease in total shaft displacement of 0.62% with ‘Flexible’ bearings at ‘Rated’ conditions under Scenario 2.

3.2. Comparison of ASE Computational Analyses

To evaluate the computational efficiency of the onshore, aero-servo-elastic model of the IEA-15MW-RWT produced in QBlade for this paper, equivalent simulations were run on the Monopile IEA-15MW-RWT and the floating, UMaine VoltturnUS-S variants at ‘Rated’ wind conditions. The VoltturnUS-S RWT model features a semi-submersible, floating platform developed for the IEA-15MW-RWT in a collaboration between the University of Maine and the National Renewable Energy Laboratory (NREL) [35], both are pictured in Figure 20 below. The platform features a central column used to mount the turbine, and three radial columns, each held in place by a mooring line.

With the wind field defined in Section 2.2 applied to each model, the offshore, fixed and floating variants were simulated under the same parameters as the simplified model, with no wave field generated. Additionally, the Monopile model was run with the offshore environment deactivated. The total normal force exerted on blade 1 of each model was then obtained for every timestep of the 10 min simulation, and the average normal force then found. The CPU processing time for each simulation is presented in Table 11.

The development of the onshore model carried out in this paper provided aerodynamic loads with a range of 3.8% and 6.5% of those obtained under the same conditions applied to the Monopile and VoltturnUS-S 15MW-RWT models, whilst reducing CPU time against them by 42% and 52%, respectively. Running the Monopile variant with the onshore option enabled was found to reduce CPU time by only 7.7%, which indicates that the

added complexity of the substructure gives rise to added computational expense, despite removing the offshore environment.

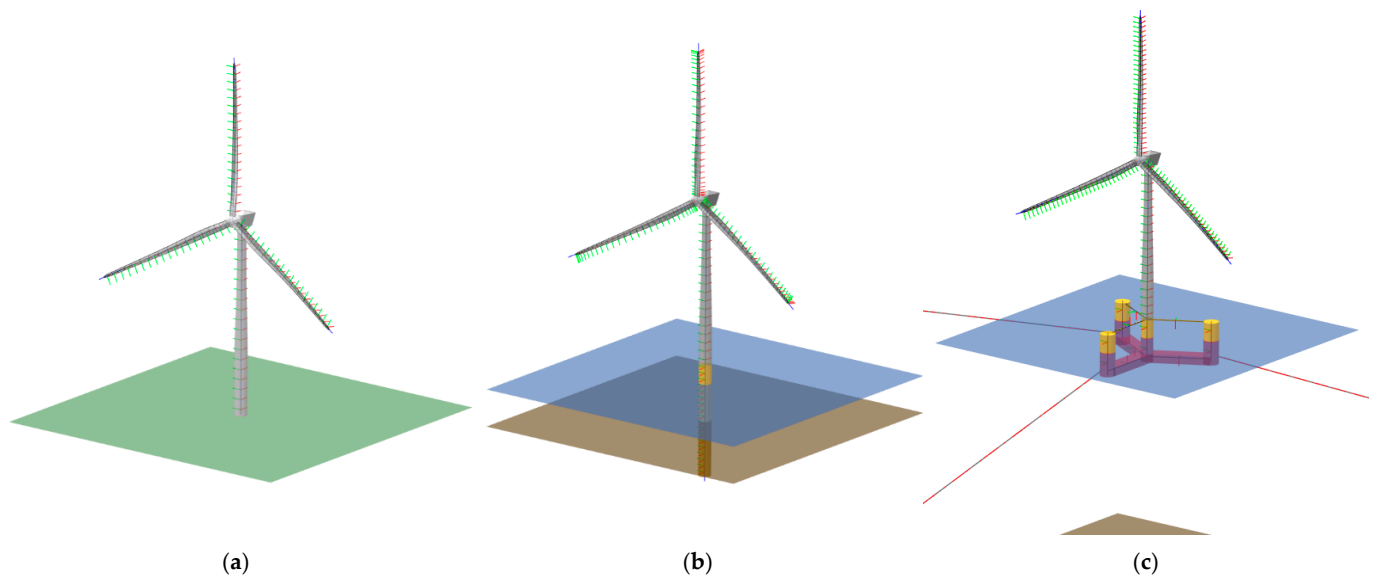


Figure 20. (a) Onshore 15 MW turbine, (b) fixed-bottom, Monopile IEA-15MW-RWT and (c) IEA-VolturnUS-S Floating 15MW RWT.

Table 11. Computational analysis comparison.

Model	Average Total Normal Force [N]	Difference [%]	CPU Processing Time [s]	Difference [%]
Simplified	607,140	-	265	-
VolturnUS-S Floating	570,085	−6.5%	553	52.1%
IEA-15MW Monopile (Offshore)	577,571	−5.1%	363	27.1%
IEA-15MW Monopile (Onshore)	585,031	−3.8%	407	35.0%

Whilst the simplified model produces higher average normal forces than its counterparts, this was found to be insignificant, and considering the aim of this work is to better inform generator deformation limits in the optimisation process, it is reasonable to assert that overestimating the impact of aerodynamic loads errs on the side of increasing safety margins by which to optimise the direct-drive structure, thus helping to prevent catastrophic failure.

3.3. Results of the Parametric Optimisation of the Generator Rotor

A high-density, tetrahedral mesh was produced using a mesh size of 140 mm, finding a mesh composition of 29,423 elements and 59,558 nodes for the starting rotor geometry, and 44,592 elements and 82,562 nodes for the structure obtained under the final loading scenario. The results of the optimisation process are presented in Table 12.

An initial analysis of the unaltered rotor found a deformation of 17.2 mm at the inner cylinder surface, increasing to 35.8 mm under Mode 2. In order to meet the original, baseline maximum deformation limit of 2.03 mm, the rotor mass increased by nearly 230%, from 84,240 kg to 277,120 kg, and the resulting rotor structure was found to exhibit 68% more deformation under Mode 2 than Mode 0.

The rotor structure resulting from optimisation under Scenario 5, the greatest normal load imbalance, the loading case with the highest shaft eccentricity without the inclusion of tangential loading, found a required mass of 338,320 kg to meet the deflection limit of

1.419 mm, an increase of 22% against the baseline deflection limit, and under Mode 0 the rotor experienced 54% lower deformation than under Mode 2.

Table 12. Result of the parametric optimisation.

	Limit [mm]	Disk Thickness [m]	Cylinder Thickness [m]	Rotor Mass [kg] (% Δ)	Mode	Inner Cylinder Def. [mm]	Eq. Stress [MPa]
Unaltered Rotor	-	0.080	0.127	84,238.3	2	35.835	66.61
				(−69.6)	0	17.199	54.22
Original Limit (Baseline)	2.03	0.364	0.188	277,116.3	2	2.021	27.45
				(−)	0	1.204	27.07
S5: High, Flexible, Normal Only	1.419	0.446	0.220	338,318.4	2	1.418	23.60
				(+22.1)	0	0.923	23.24
S4: High, Rigid, Normal and Tang.	0.901	0.554	0.359	455,052.3	2	0.897	15.87
				(+64.2)	0	0.658	15.64
S4: High, Flexible, Normal and Tang.	0.872	0.582	0.331	463,459.7	2	0.871	16.94
				(+67.2)	0	0.640	16.68

Under the highest combined normal and tangential load, scenario 4, with ‘Rigid’ bearings and a limit of 0.901 mm, the rotor mass reached 455,050 kg, an increase of 64% over the structure produced to meet the original limit. Lastly, with the strictest deformation limit of 0.872 mm, scenario 4 with ‘Flexible’ bearings, the rotor mass increased a further 8400 kg, to 463,460 kg, 67% heavier than the structural mass under the original limit. Operation under Mode 0 loading was found to decrease deformation by 36% for the scenario 4 rotors with ‘Rigid’ and ‘Flexible’ bearings, respectively.

4. Discussion

The development of the onshore IEA 15MW RWT model provided the ability to isolate and simulate the transmission of normal and tangential aerodynamic blade loads to the generator and evaluate their effects on generator structural integrity, in a computationally efficient manner, minimising overall processing time.

The aerodynamic loading was simulated using QBlade, a widely used and industry-standard software tool. While this study does not include direct comparison with field data, a previous study [20] demonstrated good agreement between the wind fields generated within QBlade and offshore wind farm weather data provided by Ørsted, ensuring that the aerodynamic loads experienced by the turbine are consistent with real weather conditions at offshore wind farm sites. Whilst in relatively close agreement with each other, some minor differences in the set-up of QBlade structural models and controller files may explain the margin of errors shown in the average normal blade loading obtained from the aero-servo-elastic simulations. These differences are acceptable, however, and confirm the model can be used to reliably inform subsequent analyses.

Bichan et al. [36] found that shaft eccentricity is greater under rated conditions than at high conditions. This work, its continuation, finds that not to be true, and that the lower level of shaft eccentricity at high windspeeds seen in [36] is a consequence of the increased blade pitch required to maintain the rated rotor speed, reducing normal load and increasing tangential loading. The incorporation of tangential loading in the structural simulation provides further value and clarity on the airgap variance experienced by the generator as a result of aerodynamic loading on the blades. With ‘High’ windspeeds, the final timestep shows the importance of tangential loading, as the maximum shaft and generator area displacements and generator area maximum Von Mises stress was shown to increase by factors of over 10, and whilst these values are far from the worst-case loading scenario, the effect may be significant when evaluating structural fatigue life limits. Furthermore, the

perceived worst-case loading scenario with regards to generator area displacement was found to be the timestep with the highest combined normal and tangential loads across the rotor plane at 'High' windspeeds; should tangential loading have been excluded from this analysis, the effects of aerodynamic loading would have been underestimated by 106%, given that the worst displacement excluding tangential loading is obtained from Scenario 5 at 'High' windspeeds, with shaft eccentricities of 27.4%, and including tangential loads, the worst-case becomes scenario 2, and a shaft eccentricity of 56.4%. The inclusion of tangential loading was found to decrease the maximum structural deformation limit of the generator rotor by 38.5%, from 1.419 mm to 0.872 mm.

Due to the absence of the required publicly available stiffness data for bearings at the scale required for a 15 MW turbine, bearing stiffness values in this study were estimated by extrapolating from smaller-scale bearings. The limitations of this approach are acknowledged, though it provides a necessary and reasonable approximation in the context of large-scale turbine modelling where empirical data is currently unavailable.

This work finds that the inclusion of 'Flexible' bearings increased maximum generator area displacement by as much as 10.8%, under Scenario 1, 'High' operating conditions, with normal loading only, though it is worth noting this increase was a high percentage of the lowest levels of displacement obtained throughout. The increase in generator area displacement due to 'Flexible' bearings was found to be higher with the normal load imbalance than tangential load imbalance, at 9.1% versus 6.7% at 'High' windspeeds, and 7% versus 5.9% at 'Rated' conditions, indicating that a higher speed and more turbulent conditions have greater adverse effects on bearing loads, increasing radial stresses and displacements present at the bearing mounting surfaces, a fact that is supported by the literature [30,37]. Furthermore, while this work finds that imbalances in aerodynamic loading across the rotor plane are less consequential for driveshaft misalignments than the total force, the flexibility of the main bearings has the greatest impact on the displacement of the area connecting the driveshaft to the generator under high load imbalance. This confirms that the inclusion of main bearing stiffness is essential for accurately modelling aerodynamic loading effects on large-scale wind turbine drivetrains.

As the primary aim of this work is to quantify the effects of aerodynamic loading on generator structural integrity, with a secondary objective of maintaining computational efficiency, the blade structure was simplified to reduce model complexity. A sensitivity analysis using reduced blade component thicknesses showed a ~10% increase in blade tip deflection, but the resulting change in shaft deflection remained below 0.7%. This indicates that, under the conditions studied, the drivetrain-level response is not significantly sensitive to detailed blade deformation mechanics. Therefore, the adopted simplification preserves the study's focus on the generator and shaft-level structural response without materially compromising the validity of the findings.

The parametric optimisation of the rotor under the deformation limits obtained in this work found that imposing stricter structural deformation limits in order to account for tangential loading transmission to the drivetrain increased the required structural mass from 338,320 kg to 463,460 kg (37%) at Mode 2. Accounting for the stiffness of the bearings in the simplified drivetrain simulation increased the necessary structural mass of the rotor structure by 1.8%, from 455,050 kg to 463,460 kg.

This represents a significant increase in the structural requirements of the PMDD generator, which in turn increases the financial and environmental cost of the generator structure, and whilst this may be mitigated somewhat by the adoption of more sophisticated optimisation techniques, it cannot be eliminated entirely. Additionally, this study focuses on a conventional PMDD disk-supported generator configuration. While alternative topologies (e.g., conically supported and arm-supported) may offer improved lightweighting,

the disk-supported structure was selected due to its widespread use in industry and its adoption in the IEA 15 MW Reference Wind Turbine on which this work is based. The inclusion of alternative topologies lies beyond the scope of this study and would confound the primary aim of isolating aerodynamic effects. Moreover, such designs are already well addressed in the existing literature.

Regardless, the authors suggest that future studies incorporate further optimisation of the disk-supported generator structure, and exploration of alternative configurations, to better understand the full implication of aerodynamic loading on the drivetrain stability of large-scale direct-driven wind turbines.

The dynamic and electromagnetic consequences of the shaft eccentricities identified in this study on generator longevity, performance and efficiency, lie outside the scope of this structural analysis. Their importance, however, also warrants consideration in future work.

This study considers idealised conditions for material properties and component geometries, consistent with its early-stage focus on evaluating the structural effects of aerodynamic loading. Variation arising from manufacturing tolerances and material properties can influence structural response and would need to be accounted for in detailed design. As a result, the work carried out to mitigate aerodynamic loading in this study would likely lead to more conservative and therefore heavier generator structures in a real-world engineering context. Incorporating such variability would require a probabilistic framework, which lies beyond the scope of this study but represents a valuable direction for future work.

5. Conclusions

This paper first presents the development of an aero-servo-elastic model of a full-scale, onshore version of the International Energy Agency's 15MW Reference Wind Turbine. With the adaption of controller files to suit, and structural properties of the turbines' blades and tower derived from documentation available on the IEA repository on GitHub, accurate modelling of the controller and structural behaviour of the turbine in real world weather conditions was ensured. The ASE model developed in this paper was found to produce aerodynamic data within the margin of error against alternative published models, whilst reducing the computational time by over half.

Next, this paper details the design of the simplified drivetrain structure of the IEA-15MW-RWT, including a uniform blade structure allowing for the streamlined application of aerodynamic loads. Crucially to this work, this paper also details the process taken to provide accurate definitions of the IEA-15MW-RWT's two main bearings and obtain the structural stiffnesses of each. Through these means, the turbines' structural response to aerodynamic blade loading—including both normal loads and, in a first in literature, tangential loads—was evaluated through finite element analysis. An evaluation of the potential worst-case loading scenarios found that high windspeeds close to the turbine cut-out speed produced the highest aerodynamic forces, and that whilst higher normal forces produced greater shaft misalignments, the inclusion of tangential forces can greatly increase shaft misalignments. It is therefore imperative, to any efforts made to evaluate the impact of aerodynamic loading on wind turbine drivetrains, that tangential forces be included.

The process offered by this paper represents the opportunity to quantify the effects of aerodynamic loading on direct-drive, large-scale wind turbine drivetrains in a computationally efficient manner, ultimately allowing for the optimisation of the direct-drive generator rotor and stator structures to account for shaft misalignments arising from aerodynamic loads, by reducing the effective airgap deformation limit accordingly.

Given that aerodynamic loading on PMDD generator structures is a relatively unexplored external load with a large influence on direct-drive generator integrity, further

exploration of other external loading impacts on generator integrity is warranted and crucial to our understanding of the applicability of direct-drive generation in offshore wind as structures continue to scale up. Thus, future research may involve the incorporation of wave load transmission to the generator, obtained through the IEA Monopile and VoltturnUS-S floating variant models available through QBlade, and applied to a simplified, representative structure of the IEA-15MW-RWT, whilst the recently published IEA 22MW reference turbine [38] provides the opportunity to evaluate how aerodynamic and hydrodynamic loading on the generator scales with turbine rating. Additionally, the development of a method to carry out a transient FEA of blade loading on the structure would provide the means to analyse generator structure fatigue arising from aerodynamic loading.

Author Contributions: Conceptualisation, M.B. and P.J.-S.; methodology, M.B.; software, M.B.; validation, M.B. and P.J.-S.; formal analysis, M.B.; investigation, M.B.; resources, P.J.-S.; data curation, M.B.; writing—original draft preparation, M.B.; writing—review and editing, P.J.-S. and N.S.; visualisation, M.B.; supervision, N.S., P.J.-S. and F.M.-S.; project administration, P.J.-S. and N.S.; funding acquisition, P.J.-S. All authors have read and agreed to the published version of the manuscript.

Funding: This work was funded by Edinburgh Napier University under the SCEBE PhD Studentship.

Data Availability Statement: The original contributions presented in the study are included in the article, further inquiries can be directed to the corresponding author.

Acknowledgments: The authors would like to thank Julian Hammond-Miller of The Timken Company, for his feedback on the method used to calculate bearing stiffnesses.

Conflicts of Interest: The authors declare no conflicts of interest.

Abbreviations

The following abbreviations are used in this manuscript:

O&M	Operation and Maintenance
LCOE	Levelised Cost of Energy
PMDD	Permanent Magnet Direct-Drive
IEA-15MW-RWT	International Energy Agency 15MW Reference Wind Turbine
FEA	Finite Element Analysis
CAD	Computer-Aided Design
HAWT	Horizontal Axis Wind Turbine
U-BEM	Unsteady Blade Element Momentum
TDO	Tapered Double Outer
SRB	Spherical Roller Bearing
B1_TDO	Bearing 1 (Tapered Double Outer)
B2_SRB	Bearing 2 (Spherical Roller Bearing)

Appendix A

Table A1. IEA-15MW-RWT blade configuration.

IEA–15MW-RWT Blade Configuration							QBlade Blade Parameters				
	Diameter [m]	Chord [m]	Twist [deg]	X Axis Offset [m]	Y Axis Offset [m]	Position [m]	Chord [m]	Twist [deg]	IP Offset [m]	OOP Offset [m]	Foil
1	3.970	5.2000	15.5946	−0.0228	−0.0063	0.00000	5.20000	15.59	−0.0228	−0.0063	AF00
2	6.358	5.2088	15.5877	0.0501	0.0324	2.38775	5.20884	15.59	0.0501	0.0324	AF01
3	8.746	5.2379	15.4108	0.0869	0.0662	4.77551	5.23789	15.41	0.0869	0.0662	AF02
4	11.133	5.2933	14.9486	0.0531	0.0855	7.16326	5.29333	14.95	0.0531	0.0855	AF03
5	13.521	5.3673	14.2585	−0.0283	0.0964	9.55101	5.36734	14.26	−0.0283	0.0964	AF04

Table A1. Cont.

IEA – 15MW-RWT Blade Configuration						QBlade Blade Parameters					
	Diameter [m]	Chord [m]	Twist [deg]	X Axis Offset [m]	Y Axis Offset [m]	Position [m]	Chord [m]	Twist [deg]	IP Offset [m]	OOP Offset [m]	Foil
6	15.909	5.4521	13.3971	−0.1353	0.1050	11.93877	5.45209	13.40	−0.1353	0.1050	AF05
7	18.297	5.5400	12.4220	−0.2434	0.1160	14.32652	5.54003	12.42	−0.2434	0.1160	AF06
8	20.684	5.6218	11.3946	−0.3189	0.1340	16.71428	5.62182	11.39	−0.3189	0.1340	AF07
9	23.072	5.6925	10.3710	−0.3470	0.1600	19.10203	5.69253	10.37	−0.3470	0.1600	AF08
10	25.460	5.7426	9.4040	−0.3819	0.1773	21.48978	5.74261	9.40	−0.3819	0.1773	AF09
11	27.848	5.7648	8.5515	−0.4163	0.1863	23.87754	5.76484	8.55	−0.4163	0.1863	AF10
12	30.235	5.7561	7.8332	−0.4350	0.1904	26.26529	5.75612	7.83	−0.4350	0.1904	AF11
13	32.623	5.7031	7.1914	−0.4193	0.1965	28.65304	5.70310	7.19	−0.4193	0.1965	AF12
14	35.011	5.6047	6.5516	−0.3833	0.2035	31.04080	5.60468	6.55	−0.3833	0.2035	AF13
15	37.399	5.4716	5.9340	−0.3521	0.2082	33.42855	5.47156	5.93	−0.3521	0.2082	AF14
16	39.786	5.3228	5.3461	−0.3259	0.2108	35.81631	5.32278	5.35	−0.3259	0.2108	AF15
17	42.174	5.1665	4.7963	−0.3029	0.2116	38.20406	5.16648	4.80	−0.3029	0.2116	AF16
18	44.562	5.0194	4.2966	−0.2833	0.2111	40.59181	5.01942	4.30	−0.2833	0.2111	AF17
19	46.950	4.8858	3.8470	−0.2650	0.2075	42.97957	4.88581	3.85	−0.2650	0.2075	AF18
20	49.337	4.7680	3.4453	−0.2469	0.1961	45.36732	4.76796	3.45	−0.2469	0.1961	AF19
21	51.725	4.6546	3.0769	−0.2287	0.1739	47.75507	4.65457	3.08	−0.2287	0.1739	AF20
22	54.113	4.5410	2.7336	−0.2109	0.1379	50.14283	4.54103	2.73	−0.2109	0.1379	AF21
23	56.501	4.4282	2.4122	−0.1945	0.0903	52.53058	4.42818	2.41	−0.1945	0.0903	AF22
24	58.888	4.3170	2.1117	−0.1806	0.0345	54.91834	4.31696	2.11	−0.1806	0.0345	AF23
25	61.276	4.2079	1.8284	−0.1687	−0.0277	57.30609	4.20788	1.83	−0.1687	−0.0277	AF24
26	63.664	4.1016	1.5588	−0.1591	−0.0932	59.69384	4.10165	1.56	−0.1591	−0.0932	AF25
27	66.052	3.9987	1.3024	−0.1520	−0.1624	62.08160	3.99871	1.30	−0.1520	−0.1624	AF26
28	68.439	3.8994	1.0644	−0.1475	−0.2435	64.46935	3.89941	1.06	−0.1475	−0.2435	AF27
29	70.827	3.8032	0.8434	−0.1443	−0.3388	66.85710	3.80317	0.84	−0.1443	−0.3388	AF28
30	73.215	3.7094	0.6366	−0.1429	−0.4485	69.24486	3.70939	0.64	−0.1429	−0.4485	AF29
31	75.603	3.6171	0.4370	−0.1431	−0.5692	71.63261	3.61711	0.44	−0.1431	−0.5692	AF30
32	77.990	3.5256	0.2397	−0.1449	−0.6981	74.02036	3.52563	0.24	−0.1449	−0.6981	AF31
33	80.378	3.4341	0.0397	−0.1477	−0.8322	76.40812	3.43408	0.04	−0.1477	−0.8322	AF32
34	82.766	3.3419	−0.1728	−0.1512	−0.9695	78.79587	3.34193	−0.17	−0.1512	−0.9695	AF33
35	85.154	3.2487	−0.4071	−0.1552	−1.1080	81.18363	3.24868	−0.41	−0.1552	−1.1080	AF34
36	87.541	3.1561	−0.6804	−0.1596	−1.2532	83.57138	3.15611	−0.68	−0.1596	−1.2532	AF35
37	89.929	3.0646	−0.9993	−0.1642	−1.4075	85.95913	3.06458	−1.00	−0.1642	−1.4075	AF36
38	92.317	2.9730	−1.3205	−0.1685	−1.5694	88.34689	2.97299	−1.32	−0.1685	−1.5694	AF37
39	94.705	2.8807	−1.6233	−0.1724	−1.7386	90.73464	2.88071	−1.62	−0.1724	−1.7386	AF38
40	97.092	2.7870	−1.8844	−0.1755	−1.9137	93.12239	2.78697	−1.88	−0.1755	−1.9137	AF39
41	99.480	2.6910	−2.0862	−0.1785	−2.0936	95.51015	2.69103	−2.09	−0.1785	−2.0936	AF40
42	101.868	2.5920	−2.1640	−0.1819	−2.2786	97.89790	2.59197	−2.16	−0.1819	−2.2786	AF41
43	104.256	2.4893	−2.1758	−0.1856	−2.4686	100.28566	2.48932	−2.18	−0.1856	−2.4686	AF42
44	106.643	2.3839	−2.1553	−0.1893	−2.6663	102.67341	2.38392	−2.16	−0.1893	−2.6663	AF43
45	109.031	2.2759	−2.1029	−0.1925	−2.8712	105.06116	2.27592	−2.10	−0.1925	−2.8712	AF44
46	111.419	2.1655	−2.0184	−0.1950	−3.0832	107.44892	2.16547	−2.02	−0.1950	−3.0832	AF45
47	113.807	2.0526	−1.8967	−0.1971	−3.3019	109.83667	2.05263	−1.90	−0.1971	−3.3019	AF46
48	116.194	1.9378	−1.7243	−0.1990	−3.5277	112.22442	1.93775	−1.72	−0.1990	−3.5277	AF47
49	118.582	1.8197	−1.5081	−0.2003	−3.7589	114.61218	1.81966	−1.51	−0.2003	−3.7589	AF48
50	120.970	0.5000	−1.2424	−0.0591	−3.9987	116.99993	0.50000	−1.24	−0.0591	−3.9987	AF49

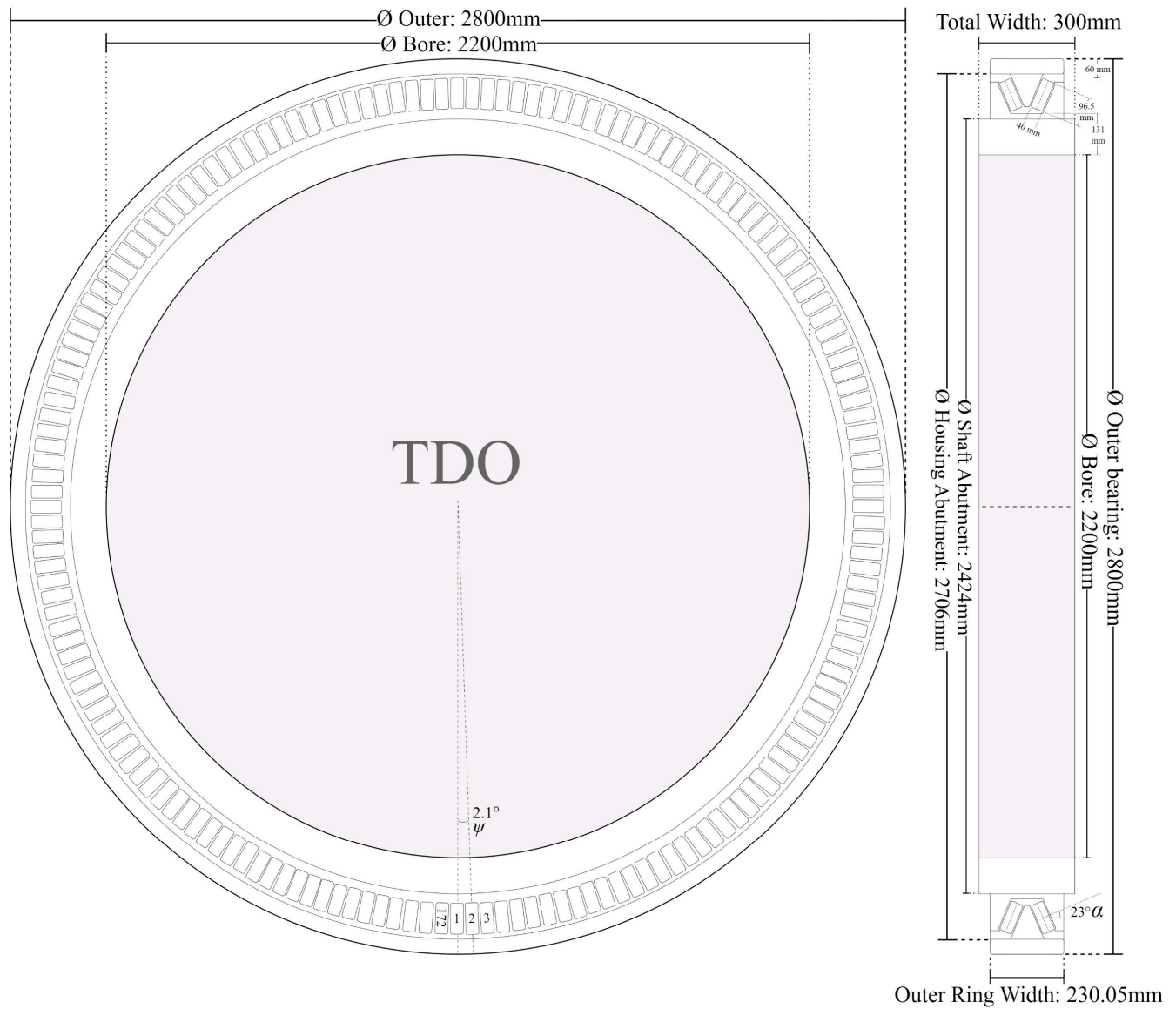


Figure A1. Technical drawing of Bearing 1—tapered double outer.

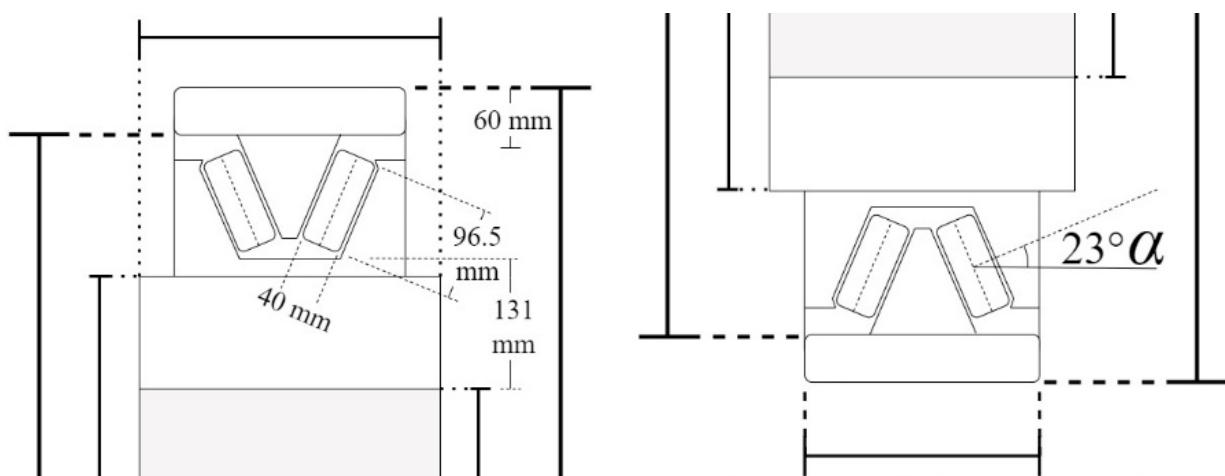


Figure A2. Bearing 1—TDO technical drawing details.

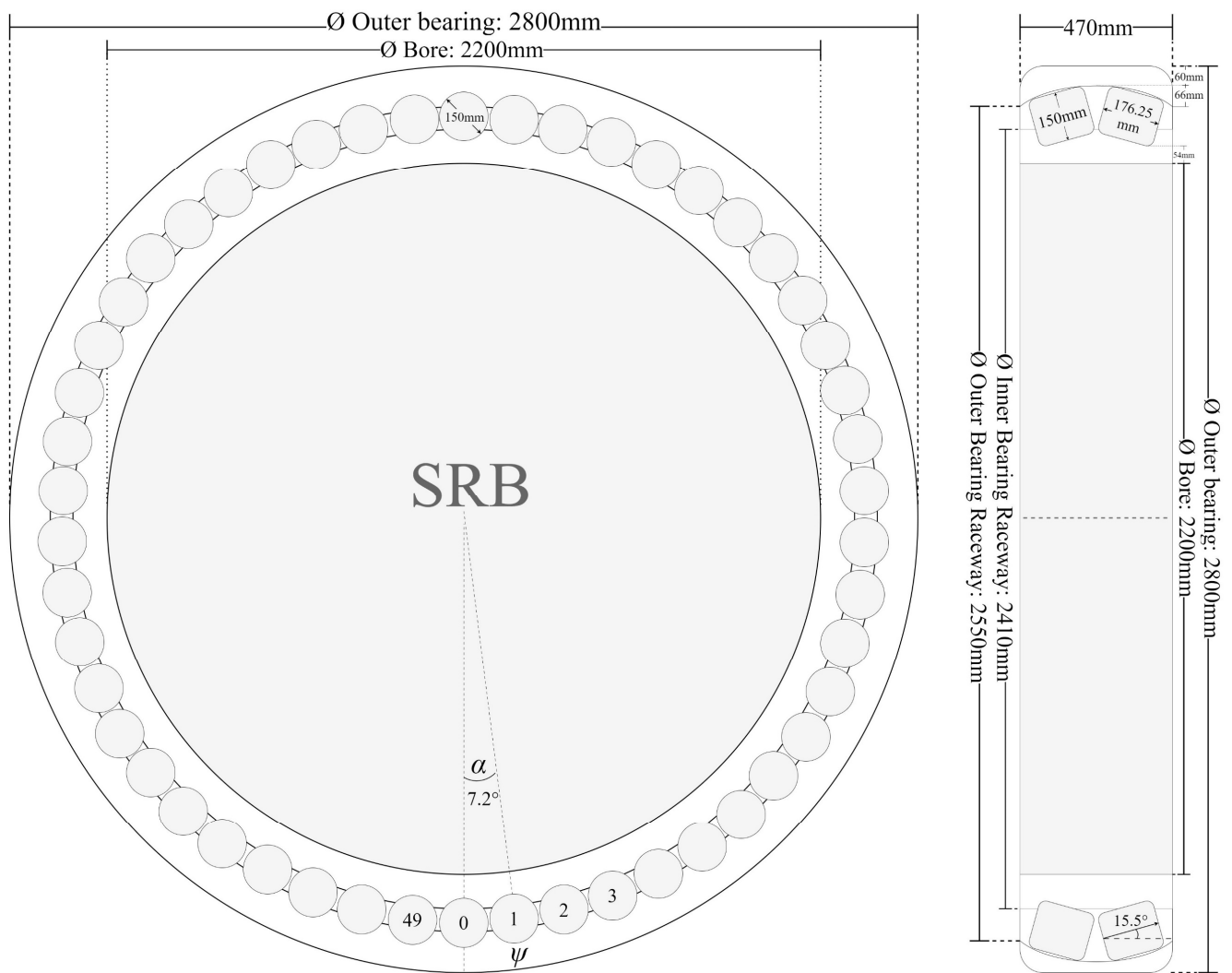


Figure A3. Technical drawing of Bearing 2—spherical roller bearing.

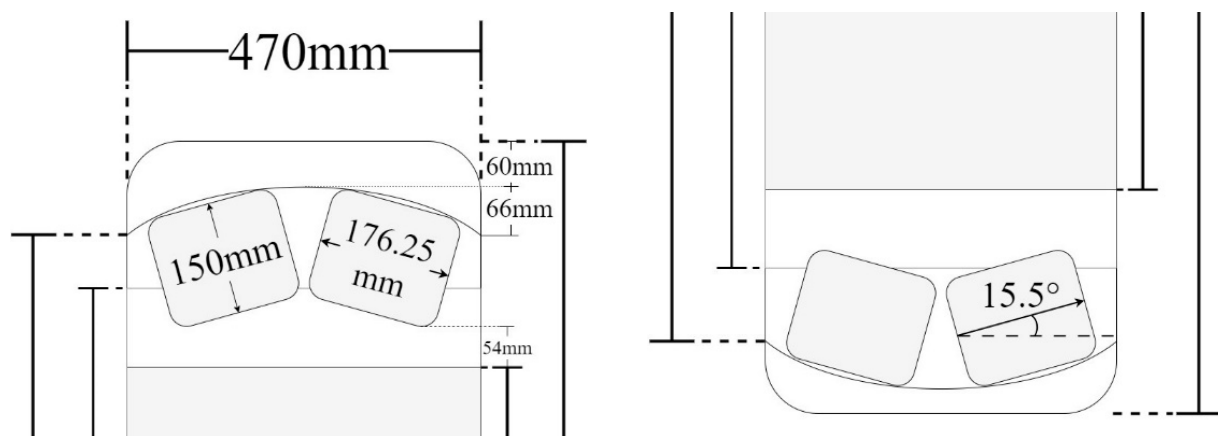


Figure A4. Bearing 2—SRB technical drawing details.

References

1. BloombergNEF Global Low-Carbon Energy Technology Investment Surges Past \$1 Trillion for the First Time. BNEF 2023. Available online: <https://about.bnef.com/blog/global-low-carbon-energy-technology-investment-surges-past-1-trillion-for-the-first-time/> (accessed on 11 June 2024).
2. Costanzo, G.; Brindley, G.; Willems, G.; Ramirez, L.; Cope, P.; Klonari, V. *Wind Energy in Europe: 2023 Statistics and the Outlook for 2024–2030*; O’Sullivan, R., Ed.; WindEurope: Brussels, Belgium, 2024.
3. Department for Energy Security & Net Zero. *Electricity Generation Costs 2023*; Department for Energy Security & Net Zero: London, UK, 2023. Available online: <https://assets.publishing.service.gov.uk/media/6556027d046ed400148b99fe/electricity-generation-costs-2023.pdf> (accessed on 28 April 2024).
4. Kaiser, M.J.; Snyder, B.F. *Offshore Wind Energy Cost Modeling*; Springer: London, UK, 2012; ISBN 9781608054220.
5. DESNZ Renewable Energy Planning Database (REPD): July 2024. Available online: <https://www.gov.uk/government/publications/renewable-energy-planning-database-monthly-extract> (accessed on 16 August 2024).
6. BEIS. *Renewable Energy Planning Database (REPD): April 2023*; BEIS: London, UK, 2023. Available online: <https://www.gov.uk/government/publications/renewable-energy-planning-database-monthly-extract> (accessed on 3 July 2023).
7. Durakovic, A. First Siemens Gamesa 14.7 MW Turbine Stands at Moray West Offshore Wind Farm. Offshore WIND 2024. Available online: <https://www.offshorewind.biz/2024/04/22/first-siemens-gamesa-14-7-mw-turbine-stands-at-moray-west-offshore-wind-farm/> (accessed on 10 May 2024).
8. GE Vernova GE’s Haliade-X 14.7 MW-220 Turbine Obtains Full DNV Type Certificate 2022. Available online: <https://www.ge.com/news/taxonomy/term/2152> (accessed on 11 September 2024).
9. Nield, D. The Largest and Most Powerful Wind Turbine Ever Built Is Now Operational. ScienceAlert 2023. Available online: <https://www.sciencealert.com/the-largest-and-most-powerful-wind-turbine-ever-built-is-now-operational> (accessed on 2 May 2024).
10. Ren, Z.; Verma, A.S.; Li, Y.; Teuwen, J.J.; Jiang, Z. Offshore Wind Turbine Operations and Maintenance: A State-of-the-Art Review. *Renew. Sustain. Energy Rev.* **2021**, *144*, 110886. [CrossRef]
11. Nejad, A.R.; Keller, J.; Guo, Y.; Sheng, S.; Polinder, H.; Watson, S.; Dong, J.; Qin, Z.; Ebrahimi, A.; Schelenz, R.; et al. Wind Turbine Drivetrains: State-of-the-Art Technologies and Future Development Trends. *Wind Energy Sci.* **2022**, *7*, 387–411. [CrossRef]
12. Dalgic, Y.; Lazakis, I.; Turan, O. Vessel Charter Rate Estimation for Offshore Wind O&M Activities. In Proceedings of the 15th International Congress of the International Maritime Association of the Mediterranean IMAM, Coruna, Spain, 14–17 October 2013; pp. 899–908.
13. Dao, C.; Kazemtabrizi, B.; Crabtree, C. Wind Turbine Reliability Data Review and Impacts on Levelised Cost of Energy. *Wind Energy* **2019**, *22*, 1655–1890. [CrossRef]
14. Hayes, A.; Sethuraman, L.; Dykes, K.; Fingersh, L.J. Structural Optimization of a Direct-Drive Wind Turbine Generator Inspired by Additive Manufacturing. *Procedia Manuf.* **2018**, *26*, 740–752. [CrossRef]
15. Hayes, A.C.; Whiting, G.L. Reducing the Structural Mass of Large Direct Drive Wind Turbine Generators through Triply Periodic Minimal Surfaces Enabled by Hybrid Additive Manufacturing. *Clean Technol.* **2021**, *3*, 227–242. [CrossRef]
16. Tartt, K.; Amiri, A.K.; McDonald, A.; Jaen-Sola, P. Structural Optimisation of Offshore Direct-Drive Wind Turbine Generators Including Static and Dynamic Analyses. *J. Phys. Conf. Ser.* **2021**, *2018*, 012040. [CrossRef]
17. Jaen-Sola, P.; Oterkus, E.; McDonald, A.S. Parametric Lightweight Design of a Direct-Drive Wind Turbine Electrical Generator Supporting Structure for Minimising Dynamic Response. *Ships Offshore Struct.* **2021**, *16*, 266–274. [CrossRef]
18. Marten, D.; Saverin, J.; Perez-Becker, S.; Behrens de Luna, R. QBlade CE 2023 (v 2.0.5.1). Available online: <https://qblade.org/> (accessed on 10 April 2023).
19. BOVIA Dassault Systèmes. BOVIA Solidworks; 2022 (v 29.3.0.0059). Available online: <https://www.solidworks.com/> (accessed on 10 April 2023).
20. Szatkowski, S.; Jaen-Sola, P.; Oterkus, E. An Efficient Computational Analysis and Modelling of Transferred Aerodynamic Loading on Direct-Drive System of 5 MW Wind Turbine and Results Driven Optimisation for a Sustainable Generator Structure. *Sustainability* **2024**, *16*, 545. [CrossRef]
21. Gaertner, E.; Rinker, J.; Sethuraman, L.; Zahle, F.; Anderson, B.; Barter, G.; Skrzypinski, W. *Definition of the IEA 15 MW Offshore Reference Wind Turbine*; National Renewable Energy Laboratory. NREL/TP-5000-75698: Golden, CO, USA, 2020. Available online: <https://docs.nrel.gov/docs/fy20osti/75698.pdf> (accessed on 9 January 2023).
22. Ghafoorian, F.; Enayati, E.; Mirmotahari, S.R.; Wan, H. Self-Starting Improvement and Performance Enhancement in Darrieus VAWTs Using Auxiliary Blades and Deflectors. *Machines* **2024**, *12*, 806. [CrossRef]
23. Ghafoorian, F.; Wan, H.; Chegini, S. A Systematic Analysis of a Small-Scale HAWT Configuration and Aerodynamic Performance Optimization Through Kriging, Factorial, and RSM Methods. *J. Appl. Comput. Mech* **2024**, *3*, 1–17. [CrossRef]
24. Glauert, H. *Aerodynamic Theory. Chapter 3: Airplane Propellers*, 1st ed.; Springer: Berlin/Heidelberg, Germany, 1935; ISBN 978-3-642-91487-4.

25. Snel, H.; Houwink, R.; Piers, W.J. Sectional Prediction of 3D Effects for Separated Flow on Rotating Blades. In Proceedings of the Eighteenth European Rotorcraft Forum, National Aerospace Laboratory, NL, Avignon, France, 21 September 1992.
26. Gaertner, E.; Rinker, J.; Sethuraman, L.; Zahle, F.; Anderson, B.; Barter, G.; Abbas, N.; Meng, F.; Bortolotti, P.; Skrzypinski, W.; et al. IEA-15-240-RWT: 15MW Reference Wind Turbine Repository; 2020. Available online: <https://github.com/IEAWindSystems/IEA-15-240-RWT> (accessed on 10 April 2023).
27. Hansen, M.H.; Henriksen, L.C. *Basic DTU Wind Energy Controller*; DTU Wind Energy: Roskilde, Denmark, 2013; ISBN 9788792896278.
28. Kelley, N.; Jonkman, B. TurbSim; NREL 2012. Available online: <https://www.nrel.gov/wind/nwtc/turbsim.html> (accessed on 25 January 2024).
29. Toupin, R.A. On St. Venet's Principle. In *Proceedings of the Applied Mechanics*; Springer: Berlin/Heidelberg, Germany, 1966; pp. 151–152.
30. Sethuraman, L.; Xing, Y.; Venugopal, V.; Gao, Z.; Mueller, M.; Moan, T. A 5 MW Direct-Drive Generator for Floating Spar-Buoy Wind Turbine: Drive-Train Dynamics. *Proc. Inst. Mech. Eng. C J. Mech. Eng. Sci.* **2017**, *231*, 744–763. [CrossRef]
31. Zhang, H.; Shi, W.; Liu, G.; Chen, Z. A Method to Solve the Stiffness of Double-Row Tapered Roller Bearing. *Math. Probl. Eng.* **2019**, *2019*. [CrossRef]
32. Zhang, F.; Lv, H.; Han, Q.; Li, M. The Effects Analysis of Contact Stiffness of Double-Row Tapered Roller Bearing under Composite Loads. *Sensors* **2023**, *23*, 4967. [CrossRef] [PubMed]
33. SKF. SKF® Product Catalogue: Rolling Bearings. Available online: <https://www.skf.com/uk/products/rolling-bearings> (accessed on 14 December 2023).
34. Gargiulo, E.P., Jr. A Simple Way to Estimate Bearing Stiffness. *Mach. Des.* **1980**, *52*, 107–110.
35. Allen, C.; Viselli, A.; Dagher, H.; Goupee, A.; Gaertner, E.; Abbas, N.; Hall, M.; Barter, G. *Definition of the UMaine VoltturnUS-S Reference Platform Developed for the IEA Wind 15-Megawatt Offshore Reference Wind Turbine*; National Renewable Energy Laboratory. NREL/TP-5000-76773; Golden, CO, USA, 2020.
36. Bichan, M.; Jaen-Sola, P.; Sellami, N.; Muhammad-Sukki, F. Aero-Servo-Elastic Simulation of the International Energy Agency's 15MW Reference Wind Turbine for Direct-Drive Generator Integrity Modelling. In Proceedings of the ASWEC 2024, Edinburgh, Scotland, UK, 31 July 2024.
37. Sethuraman, L.; Venugopal, V.; Zavvos, A.; Mueller, M. Structural Integrity of a Direct-Drive Generator for a Floating Wind Turbine. *Renew. Energy* **2014**, *63*, 597–616. [CrossRef]
38. Zahle, F.; Barlas, A.; Lønbaek, K.; Bortolotti, P.; Zalkind, D.; Wang, L.; Labuschagne, C.; Sethuraman, L.; Barter, G. *Definition of the IEA Wind 22-Megawatt Offshore Reference Wind Turbine*; Technical University of Denmark (DTU), Department of Wind and Energy Systems: Roskilde, Denmark, 2024. [CrossRef]

Disclaimer/Publisher's Note: The statements, opinions and data contained in all publications are solely those of the individual author(s) and contributor(s) and not of MDPI and/or the editor(s). MDPI and/or the editor(s) disclaim responsibility for any injury to people or property resulting from any ideas, methods, instructions or products referred to in the content.